Structural and Multidisciplinary Optimization (2021) 63:1863–1887
https://doi.org/10.1007/s00158-020-02784-0

RESEARCH PAPER

Topology optimization of shape memory polymer structures with programmable morphology

Anurag Bhattacharyya[1] · **Kai A. James**[1]

Received: 1 January 2020 / Revised: 23 October 2020 / Accepted: 5 November 2020 / Published online: 21 February 2021

Abstract

We present a novel optimization framework for optimal design of structures exhibiting memory characteristics by incorporating shape memory polymers (SMPs). SMPs are a class of memory materials capable of undergoing and recovering applied deformations. A finite-element analysis incorporating the additive decomposition of small strain is implemented to analyze and predict temperature-dependent memory characteristics of SMPs. The finite element method consists of a viscoelastic material modelling combined with a temperature-dependent strain storage mechanism, giving SMPs their characteristic property. The thermo-mechanical characteristics of SMPs are exploited to actuate structural deflection to enable morphing toward a target shape. A time-dependent adjoint sensitivity formulation implemented through a recursive algorithm is used to calculate the gradients required for the topology optimization algorithm. Multimaterial topology optimization combined with the thermo-mechanical programming cycle is used to optimally distribute the active and passive SMP materials within the design domain. This allows us to tailor the response of the structures to design them with specific target displacements, by exploiting the difference in the glass-transition temperatures of the two SMP materials. Forward analysis and sensitivity calculations are combined in a PETSc-based optimization framework to enable efficient multi-functional, multimaterial structural design with controlled deformations.

Keywords Multimaterial topology optimization · Shape memory polymers · Multi-physics design · Adjoint sensitivity analysis · High-performance computing

1 Introduction

Nature has always been a source of inspiration to push forward the frontiers of science and technology. One of the complex and interesting phenomena which has widely been mimicked is the shape changing or morphing phenomenon (Siéfert et al. 2019; Oliver et al. 2016). From an aerospace engineering point of view, the concept of morphing has gained momentum because of its potential to push the limits of the current flight technologies and make them more efficient. A wide range of smart materials capable of producing structural morphing has been studied and many more are currently under investigation. Shape memory materials have shown promising results in this respect.

Shape memory materials (SMM) are materials capable of recovering their original shape in the presence of the right stimulus after being quasi-plastically deformed. Two widely known types of SMMs are shape memory alloys (SMA) and shape memory polymers (SMPs). From an engineering perspective, tailoring the shape and other properties of polymers is much easier as compared to metals. This, along with other advantages mentioned in later paragraphs, motivated the current research to computationally design structures using SMPs to tailor their motion to fulfil specific design objectives.

Shape memory polymers are a class of multi-phase materials which have the ability to regain their original (permanent) shape from a deformed shape (temporary shape) as a result of a shape memory recovery process. The shape memory recovery process can be induced by a variety of stimuli like heat, light, electricity, or magnetism. The main advantages of SMPs compared to metallic shape memory alloys are substantially higher elongations,

Responsible Editor: Seonho Cho

✉ Kai A. James
kaijames@illinois.edu

[1] University of Illinois Urbana-Champaign, Urbana, IL 61801, USA

lower density, biodegradability, and the ability to be easily manufactured and given complex shapes through 3D printing technology. All these factors have made SMPs widely used in variety of applications, and particularly suited for aerospace applications (Behl and Lendlein 2011).

SMPs have been successfully used in developing self-deploying sun-rails or antennas for spacecrafts and satellites (Liu et al. 2014). The deployable panels are connected to SMP hinges that are deformed when storage and transportation are required but when exposed to heat they come back to their original undeformed state, thereby deploying the panels. SMP composites have also been investigated for wing morphing applications (Reed et al. 2005; Leng et al. 2010; Yu et al. 2009). Wache et al. prototyped and tested SMP stents using the natural body temperature for activation (Wache et al. 2003). Reconfigurable drug-delivery devices made of SMPs, capable of self-assembling, have also been studied (Cho et al. 2010). Heat-triggered movements of SMPs were also investigated to design snap-fit mechanisms to allow for easier disassembly in the production/packaging sector (Carrell et al. 2011).

A variety of experimental and constitutive modelling techniques for SMPs have already been investigated to better understand the thermo-mechanical characteristics of SMPs. Due to a growing interest in SMPs, a lot of experimental work to characterize their behavior has been carried out (Liu et al. 2006; Lendlein et al. 2005; Volk et al. 2011). Simultaneously, development of constitutive modelling techniques to predict and describe SMP behavior accurately has also been extensively investigated (Qi et al. 2008; Chen and Lagoudas 2008a, b; Baghani et al. 2012; Reese et al. 2010). Studies have been carried out to combine SMP modelling techniques with 4D printing to design active origami structures which can morph into specific target shapes (Ge et al. 2016; Tibbits 2014).

The potential of SMPs can be exploited to design morphing structures with specific tailored output motion through computational design techniques. Isogeometric configuration design optimization has been investigated to synthesize lattice structures with SMPs (Choi and Cho 2018). Topology optimization techniques have also been implemented to design multimaterial non-intuitive structures with specific objective functions for different material models (Bendsøe and Sigmund 1999; James and Waisman 2015; Carbonari et al. 2008; Gaynor et al. 2014). It has been successfully investigated to design structures with SMAs and other smart materials with multi-physics characteristics (Sigmund and Torquato 1999; Frecker 2003; Silva and Kikuchi 1999; Bowen et al. 2014; Rupp et al. 2009; Yin and Ananthasuresh 2002; Langelaar and van Keulen 2008; Langelaar et al. 2011). Level-set topology optimization has been utilized to design morphing structures with active materials and to determine the material interfaces in printed active composites (PACs) consisting of SMPs (Maute et al. 1402). Recent studies have also explored the use of the extended finite element method (XFEM) combined with the level-set method to design self-actuating, shape-changing structures, capable of undergoing large deformations (Geiss and Maute 2018; Geiss et al. 2019). This approach enables explicit representation of the material boundary to better exploit emerging additive manufacturing technologies. The current study aims to further expand the scope of the application of topology optimization framework to design morphing structures through continuous distribution of multiple SMP materials throughout the design domain to be able to design mechanisms and multi-functional structures with complex motions.

This paper proposes a novel optimization framework to harness the potential of SMPs to design structures with specific target displacements via topology optimization. The multi-physics SMP behavior has been simulated using MATLAB- and PETSc-based implementations. The current study includes a unique attempt to implement a time-dependent adjoint sensitivity analysis for SMP structures, and uses the gradient information to computationally design shape-changing structures through topology optimization. We propose a novel, computationally efficient, thermo-mechanical programming cycle for SMPs, and using this technique several multimaterial topology optimization designs for morphing structures are presented.

2 Thermo-mechanical programming cycle

The SMP mechanics are governed by the characteristics of its constituent phases namely a rubbery phase and a

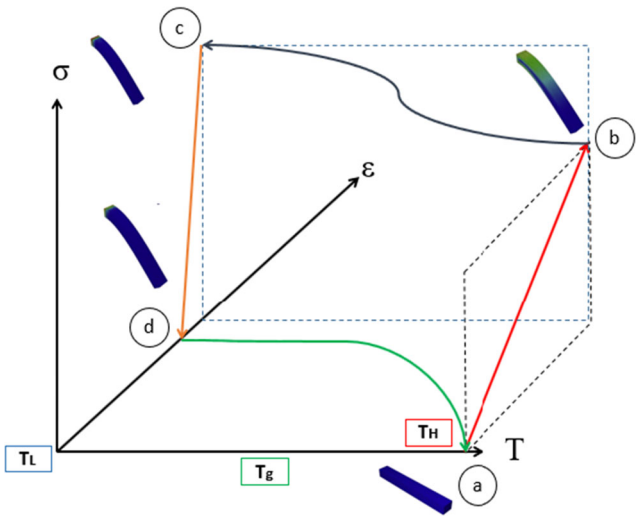

Fig. 1 Thermo-mechanical programming cycle for SMPs

glassy phase. The thermo-mechanical programming cycle is responsible for making SMPs exhibit their shape memory characteristics. When the temperature during the thermo-mechanical cycle changes from the maximum temperature (T_H) to the minimum temperature (T_L), the volume fraction of the rubbery and glassy phases changes, changing the structural behavior of the polymer and imparting it with memory characteristics. Figure 1 shows the thermo-mechanical cycle for programming SMPs on a stress (σ)-strain (ε)-temperature (T) axis frame. Initially, the structure is in state (a) at the maximum temperature (T_H) where the material is primarily in the rubbery phase. Then, keeping the temperature constant, it is deformed from state (a) to state (b). After being deformed to the required shape, the strain is kept constant and the temperature is decreased from T_H to T_L . As the temperature is reduced, the internal stress increases from state (b) to state (c). While going from T_H to T_L, the structure passes through the *glass transition* temperature (T_g). Before reaching T_g, most of the polymer is in the rubbery phase and after crossing T_g most of the material switches to a glassy phase which has higher stiffness than the rubbery phase. At state (c), the external applied forces are removed and the material is allowed to relax, during which time the internal stresses reduce to 0 at state (d). State (d) is the temporary shape of the structure and it can stay in this state until heated. Finally, the structure is heated back to T_H after which it regains its original undeformed shape (a). Since the recovery of its original undeformed configuration happens with the no internal stresses, this cycle is called the *stress free strain recovery* cycle.

3 Small-strain finite element analysis

The FEA model implemented in this study is based on the SMP small-strain constitutive model as proposed by Baghani et al. (2012). In this algorithmic implementation, we have not considered geometric nonlinearity.

Using the concept of additive decomposition of small strains, the total strain, $\boldsymbol{\varepsilon}$, can be split into components as:

$$\boldsymbol{\varepsilon} = \phi^g \boldsymbol{\varepsilon}^g + \phi^r \boldsymbol{\varepsilon}^r + \boldsymbol{\varepsilon}^i + \boldsymbol{\varepsilon}^T + \boldsymbol{\varepsilon}^{is} \tag{1}$$

Here, ϕ^g and ϕ^r refer to the glassy-phase volume fraction and rubbery-phase volume fraction, respectively. The volume fractions of the rubbery phase (ϕ^r) and the glassy phase (ϕ^g) are related by:

$$\phi^g + \phi^r = 1 \tag{2}$$

Terms $\boldsymbol{\varepsilon}^g, \boldsymbol{\varepsilon}^r, \boldsymbol{\varepsilon}^i, \boldsymbol{\varepsilon}^T$, and $\boldsymbol{\varepsilon}^{is}$ in the rheological model shown in Fig. 2 refer to the glassy-phase strain, strain in the rubbery phase, the inelastic strain component, the thermal strain, and the stored strain. The strain in the rubbery ($\boldsymbol{\varepsilon}^r$) and glassy ($\boldsymbol{\varepsilon}^g$) phases can be further spilt into the inelastic and elastic strain components as shown below.

$$\begin{aligned} \boldsymbol{\varepsilon}^r &= \boldsymbol{\varepsilon}^{er} + \boldsymbol{\varepsilon}^{ir} \\ \boldsymbol{\varepsilon}^g &= \boldsymbol{\varepsilon}^{eg} + \boldsymbol{\varepsilon}^{ig} \end{aligned} \tag{3}$$

The time-continuous inelastic strain evolution equations are defined by:

$$\begin{aligned} \dot{\boldsymbol{\varepsilon}}^{ir} &= \frac{\mathbb{K}_r^{neq}}{\eta_r} : (\boldsymbol{\varepsilon}^r - \boldsymbol{\varepsilon}^{ir}) \\ \dot{\varepsilon}^{ig} &= \frac{\mathbb{K}_g^{neq}}{\eta_g} : (\boldsymbol{\varepsilon}^g - \boldsymbol{\varepsilon}^{ig}) \\ \dot{\varepsilon}^{i} &= \frac{1}{\eta_i}\boldsymbol{\sigma} \end{aligned} \tag{4}$$

Here, $\mathbb{K}^{neq}$ represents the stiffness contribution of the non-equilibrium branch of the respective phases, η refers to the viscosity coefficient of the phases, and $\boldsymbol{\sigma}$ refers to the total internal stress.

The evolution equations describing the stored strain components are defined by:

$$\begin{aligned} \dot{\boldsymbol{\varepsilon}}^{is} &= \dot{\phi}^g \boldsymbol{\varepsilon}^r \ \textit{Cooling phase} \\ \dot{\boldsymbol{\varepsilon}}^{is} &= \dot{\phi}^g \frac{\boldsymbol{\varepsilon}^{is}}{\phi^g} \ \textit{Heating phase} \end{aligned} \tag{5}$$

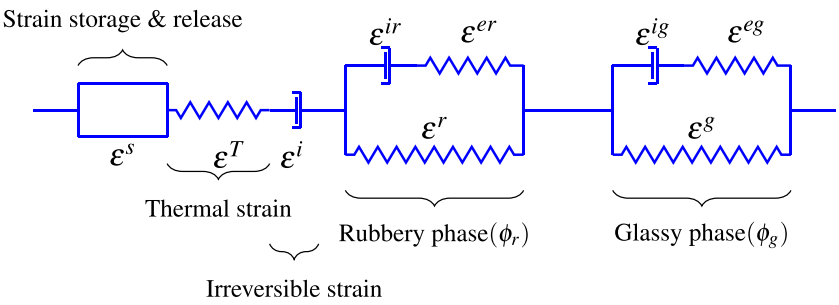

Fig. 2 The rheological model of shape memory polymer

In the constitutive modelling and verification, as provided in Appendix section, of a single SMP material, the evolution of the volume fraction of the glassy phase is given by:

$$\phi_g = 1 - \frac{1}{1 + 2.76 \times 10^{-5}(T_{max} - T)^4} \tag{6}$$

Here, T_{max} is the maximum temperature of the thermo-mechanical programming cycle and T is the temperature during any step of the thermo-mechanical process. For two SMP material topology optimization algorithm, since the materials have different glass-transition temperatures (T_g), the volume fraction of the second SMP material is calculated by:

$$\phi_g = 1 - \frac{1}{1 + \exp\left(-0.66(T - T_g)\right)} \tag{7}$$

The thermal strains in the structure are calculated by:

$$\boldsymbol{\varepsilon}^T = (\alpha_1(T - T_h) + \alpha_2(T^2 - T_h^2))\mathbf{1} \tag{8}$$

Here, α_1 and α_2 for a two-material topology optimization formulation are given in Table 1. The term $\mathbf{1}$ denotes the identity tensor. The evolution equations are converted from a time-continuous form to discrete time-stepping equations by applying a backward-Euler differencing scheme. As a result of this conversion, the evolution equations can be defined as:

$$\begin{aligned}
\boldsymbol{\varepsilon}_n^{ir} &= \mathbb{H}_r^{-1} : \boldsymbol{\varepsilon}_{n-1}^{ir} + \mathbb{W}_r : \boldsymbol{\varepsilon}_n^r \\
\boldsymbol{\varepsilon}_n^{ig} &= \mathbb{H}_g^{-1} : \boldsymbol{\varepsilon}_{n-1}^{ig} + \mathbb{W}_g : \boldsymbol{\varepsilon}_n^g \\
\boldsymbol{\varepsilon}_n^{i} &= \boldsymbol{\varepsilon}_{n-1}^{i} + \mathbb{M} : \boldsymbol{\varepsilon}_n^r - \mathbb{N} : \boldsymbol{\varepsilon}_{n-1}^{ir} \\
\boldsymbol{\varepsilon}_n^{is} &= \boldsymbol{\varepsilon}_{n-1}^{is} + \mathbb{P} : \boldsymbol{\varepsilon}_n^r \\
\boldsymbol{\varepsilon}_n^{g} &= \mathbb{O} : \boldsymbol{\varepsilon}_n^r + \mathbb{E} : \boldsymbol{\varepsilon}_{n-1}^{ir} + \mathbb{F} : \boldsymbol{\varepsilon}_{n-1}^{ig}
\end{aligned} \tag{9}$$

where the terms $\mathbb{W}_r$, $\mathbb{W}_g$, $\mathbb{M}$, $\mathbb{N}$, $\mathbb{P}$, $\mathbb{H}_r$, $\mathbb{H}_g$, $\mathbb{O}$, $\mathbb{E}$, and $\mathbb{F}$ are defined in (A.2) and (A.1). In the derivation of (9), it has been assumed that the stresses in the glassy and rubbery phases are equal. The subscript, n, represents the time step. The total strain in the rubbery phase can be calculated by:

$$\boldsymbol{\varepsilon}_{n+1}^r = \mathbb{D}_{n+1}^{-1} : \boldsymbol{C}_{n+1} \tag{10}$$

Table 1 Values of material properties

$\eta_i^{SMP^1}, \eta_i^{SMP^2}$	10,000, 15,000	MPa·min
$\eta_r^{SMP^1}, \eta_r^{SMP^2}$	1, 1.5	MPa·min
$\eta_g^{SMP^1}, \eta_g^{SMP^2}$	4000, 4500	MPa·min
$\nu_r^{SMP^1}, \nu_g^{SMP^2}$	0.4, 0.4	[−]
$\nu_g^{SMP^1}, \nu_g^{SMP^2}$	0.3, 0.3	[−]
$E_{eq}^{r\ SMP^1}, E_{eq}^{r\ SMP^2}$	0.39, 0.5	MPa
$E_{eq}^{g\ SMP^1}, E_{eq}^{g\ SMP^2}$	1100, 1500	MPa
$E_{neq}^{r\ SMP^1}, E_{neq}^{r\ SMP^2}$	0.02, 0.04	MPa
$E_{neq}^{g\ SMP^1}, E_{neq}^{g\ SMP^2}$	150, 180	MPa
$\alpha_1^{SMP^1}, \alpha_1^{SMP^2}$	-3.14×10^{-4}, -3.14×10^{-6}	K^{-1}
$\alpha_2^{SMP^1}, \alpha_2^{SMP^2}$	0.7×10^{-6}, 0.7×10^{-10}	K^{-2}

where the terms $\mathbb{D}_{n+1}$ and $\boldsymbol{C}_{n+1}$ are evaluated using:

$$\begin{aligned}
\mathbb{D}_{n+1} &= (\phi_{n+1}^r + \Delta\phi_{n+1}^g)\mathbb{I} + \phi_{n+1}^g(\mathbb{A}_g{}^{-1}\mathbb{A}_r) + \frac{\Delta t}{\eta_i}\mathbb{A}_r \\
\boldsymbol{C}_{n+1} &= \boldsymbol{\varepsilon}_{n+1} + \phi_{n+1}^g\left[\mathbb{A}_g{}^{-1} : \{-\mathbb{B}_r : \boldsymbol{\varepsilon}_n^{ir} + \mathbb{B}_g : \boldsymbol{\varepsilon}_n^{ig}\}\right] \\
&\quad -\boldsymbol{\varepsilon}_n^i + \frac{\Delta t}{\eta_i}\mathbb{B}_r : \boldsymbol{\varepsilon}_n^{ir} - \boldsymbol{\varepsilon}_n^{is} - \boldsymbol{\varepsilon}_{n+1}^T
\end{aligned} \tag{11}$$

where the terms $\mathbb{A}_r, \mathbb{A}_g, \mathbb{B}_r, \mathbb{B}_g$ and $\Delta\phi_{n+1}^g$ are defined in (A.1). The total internal stress and the tangent stiffness matrix are computed as:

$$\boldsymbol{\sigma}_{n+1} = \mathbb{A}_r : \boldsymbol{\varepsilon}_{n+1}^r - \mathbb{B}_r : \boldsymbol{\varepsilon}_n^{ir} \tag{12}$$

$$\mathbb{C}_{n+1}^{tan} = \mathbb{A}_r\mathbb{D}_{n+1}^{-1} \tag{13}$$

The residual vector $\boldsymbol{R}_{n+1}$ can be defined as:

$$\boldsymbol{R}_{n+1} = \boldsymbol{F}_{n+1}^{int} - \boldsymbol{F}_{n+1}^{ext} \tag{14}$$

$$\boldsymbol{F}^{int} = \int_\Omega \boldsymbol{B}\boldsymbol{\sigma}_{n+1}dv \tag{15}$$

where Ω refers to the whole structural domain, and $\boldsymbol{F}_{n+1}^{ext}$ is the total external force applied to the structure. The term $\boldsymbol{B}$ represents the strain-displacement matrix.

The constitutive model was implemented in a PETSc-based finite-element framework to perform structural optimization with a large number of design variables. Note that in this implementation of the constitutive model, we have assumed a uniform temperature field throughout the heating and cooling processes. This assumption reflects the slow temperature change during the thermomechanical programming cycle, and it enables us to avoid solving the coupled thermal conduction problem. Thus, at each step of the simulation, we effectively solve:

$$\nabla \cdot \sigma_n(T_n, \boldsymbol{x}) = 0 \tag{16}$$

where T_n is the temperature at time-step t_n and $\boldsymbol{x}$ refers to the position of a particular point in the design domain. The verification of the implementation of the constitutive model has been provided in the Appendix section.

4 Topology optimization

4.1 A two-material approach for SMP structural design using a modified thermo-mechanical cycle

To produce morphing shape memory polymer structures, a design approach utilizing two SMP materials with different glass-transition temperatures is used. The SMP material with the lower glass-transition temperature is hereafter referred to as the *active* SMP material and the SMP material with the higher glass-transition temperature is referred to as the *passive* SMP material. The idea is to use the

difference in the glass-transition temperature of the two SMP materials as a driving stimulus to deform the whole structure toward a specific target shape. The difference in the glass-transition temperatures would manifest as a difference in the amount of rubbery and glassy phases in the active and passive SMP materials. For a nominal amount of axial deformation, applied during the deformation step of the thermo-mechanical programming cycle, the two SMP materials will deform by different amounts, during the heating phase of the thermo-mechanical cycle, leading to the bending of the entire structure. The goal of the topology optimization algorithm is to select the distribution of the active and passive SMP materials throughout the design domain such that the deformation of the structure can be controlled to achieve specific displacements.

Due to high computational costs of the entire sensitivity analysis formulation as explained in the previous section, the thermo-mechanical cycle was shortened while preserving its essential components required for imparting shape memory characteristics to the SMP. The modified SMP programming cycle for two-material topology optimization is shown in Fig. 3. The maximum temperature (T_H) and the minimum temperature (T_L) are chosen to be 350 K and 330 K, respectively. The *glass transition temperature* ($T_g{}^a$) for the active SMP material is 340 K while that of the passive SMP material ($T_g{}^p$) is 345 K. The transition temperatures chosen here are similar to the temperatures used in SMP experimental and computational studies as provided by Baghani et al. (2012). The minimum temperature has been chosen to be 330 K to keep the temperature range small, while allowing for the full spectrum of material phases, in order to keep computational costs reasonable.

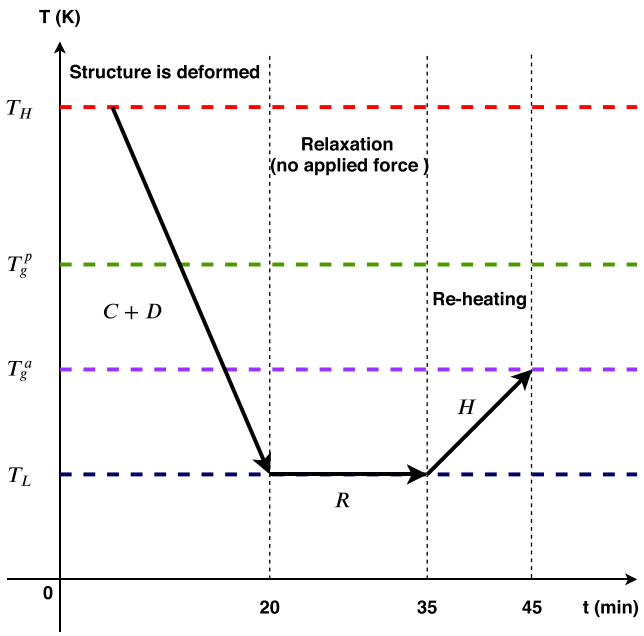

Fig. 3 Modified thermo-mechanical SMP programming cycle

Instead of deforming the structure at T_H and then cooling while keeping the strains constant, the cooling and deformation of the structure were done simultaneously. The heating and cooling rate used is ± 1 K/min. This reduced the requirement for modelling the entire thermo-mechanical cycle but at the same time kept the essential parts of the cycle to be able to successfully computationally design SMP structures with specific objectives.

The SMP thermo-mechanical programming cycle used for the numerical case studies is as follows:

- Step I: The temperature is decreased from T_H to T_L while deforming the structure with a constant load F for a total time of 20 min simulated with 4 time steps. This step is indicated with the label "C+D" in Fig. 3.
- Step II: The structure is allowed to relax without any external forces for a total time of 15 min simulated with 3 time steps. This is labeled "R" in Fig. 3.
- Step III: The structure is heated from T_L to $T_g{}^a$ over a duration of 10 min simulated with 2 time steps. This step is labeled "H" in Fig. 3.

During step III of the thermo-mechanical cycle, the structure is heated to a temperature of $T_g{}^a$, which corresponds to the glass-transition temperature of the active material. This temperature will be represented as T^* for the remainder of the paper. This results in a very high volume fraction of the glass phase in the *passive* SMP material while the glass-phase volume fraction in the active SMP material becomes considerably lower. In this way, we have selectively *activated* the shape memory response in the active material. Consequently, the active material naturally wants to return to its default shape, while the passive material wants to remain in its temporary shape. This results in an internal residual stress that can be optimally harnessed to produce complex motion that is effectively programmed into the material distribution.

4.2 Design parameterization

The main goal of topology optimization is to determine the optimal distribution of a given amount of material inside a design domain in such a way that a given objective is optimized and constraints are satisfied. To determine the optimal material distribution, finite element analysis is carried out combined with a SIMP (*solid isotropic material penalization*) scheme for material parameter interpolation. According to the SIMP formulation for a two-material interpolation (without void), the effective material properties for each element are evaluated as:

$$\Psi_{eff} = \Psi_1 + \rho^p(\Psi_2 - \Psi_1) \tag{17}$$

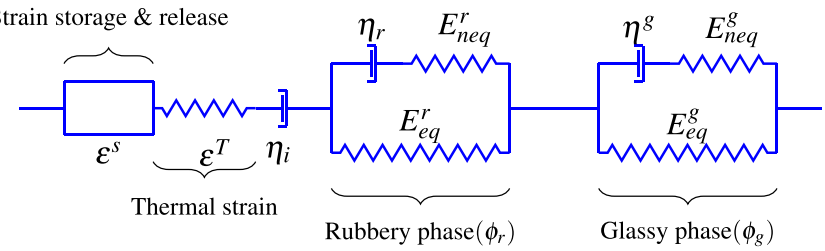

Fig. 4 Rheological model illustrating the physical significance of the SMP material properties

Here, Ψ represents a generic material parameter, ρ is the mixing ratio which ranges from 0 to 1, and p represents the penalization constant. Generally, p is chosen to be a number greater than 1 to ensure that the intermediate densities are penalized and removed from the optimal design. To avoid mesh dependency and other numerical instabilities resulting from the topology optimization method, we implement a density filtering technique as proposed by Bruns and Tortorelli (2001).

For an SMP based on the material properties as shown in Fig. 4, the SIMP formulation is used to interpolate the materials' parameters between two SMP materials, SMP^1 and SMP^2, as explained above. Equation (18) shows the SIMP interpolation scheme, modified for the two-material topology optimization framework. We investigate values of $p = 3$ and $p = 1$ for the penalization constant in the SIMP scheme of the topology optimization framework. It can be observed that only the stiffness parameters of the materials are penalized, and the other properties like viscosity coefficients (η_r, η_g) and the thermal expansion coefficients (α_1, α_2) are not penalized. This is done to guide the optimizer toward a binary solution, in which all elements exclusively contain one of the two design materials with no mixing. Table 1 lists the values of the material properties for the two SMP materials. For all the numerical examples, the convergence is based on the criterion of $|x_{k+1} - x_k| < 0.01$ as implemented in Aage et al. (2015).

$$
\begin{aligned}
\eta_i &= \eta_i^{SMP^1} + \boldsymbol{\rho}(\eta_i^{SMP^2} - \eta_i^{SMP^1}) \\
E^r_{eq} &= E^r_{eq}{}^{SMP^1} + \boldsymbol{\rho}^p(E^r_{eq}{}^{SMP^2} - E^r_{eq}{}^{SMP^1}) \\
E^r_{neq} &= E^r_{neq}{}^{SMP^1} + \boldsymbol{\rho}^p(E^r_{neq}{}^{SMP^2} - E^r_{neq}{}^{SMP^1}) \\
E^g_{eq} &= E^g_{eq}{}^{SMP^1} + \boldsymbol{\rho}^p(E^g_{eq}{}^{SMP^2} - E^g_{eq}{}^{SMP^1}) \\
E^g_{neq} &= E^g_{neq}{}^{SMP^1} + \boldsymbol{\rho}^p(E^g_{neq}{}^{SMP^2} - E^g_{neq}{}^{SMP^1}) \\
\eta_r &= \eta_r^{SMP^1} + \boldsymbol{\rho}(\eta_r^{SMP^2} - \eta_r^{SMP^1}) \\
\eta_g &= \eta_g^{SMP^1} + \boldsymbol{\rho}(\eta_g^{SMP^2} - \eta_g^{SMP^1}) \\
\alpha_1 &= \alpha_1^{SMP^1} + \boldsymbol{\rho}(\alpha_1^{SMP^2} - \alpha_1^{SMP^1}) \\
\alpha_2 &= \alpha_2^{SMP^1} + \boldsymbol{\rho}(\alpha_2^{SMP^2} - \alpha_2^{SMP^1})
\end{aligned} \tag{18}
$$

5 Time-dependent adjoint sensitivity analysis

Time-dependent adjoint sensitivity analysis is performed to calculate the gradient information required for the structural optimization process. The procedure here describes the calculation of adjoint sensitivities. The function of interest being differentiated is the displacement at a particular degree-of-freedom (a) of the structure, at a particular time step (M) as shown in Fig. 5.

Let the scalar function of interest (θ) be defined as:

$$\theta = \boldsymbol{u}_a^M(\rho) \tag{19}$$

Let $\boldsymbol{u^M(\rho)}$ represent the displacement vector of the whole structure at time step M. Then, we can write (19) as:

$$\theta = \boldsymbol{L}^T \boldsymbol{u}^M(\rho) \tag{20}$$

where $\boldsymbol{L}$ is a column vector and is zero everywhere except at the entry corresponding to the a^{th} degree-of-freedom. We can form an augmented Lagrangian function as:

$$\Theta = \theta + \sum_{i=1}^{M} \left[\boldsymbol{\lambda}^{(i)^T} \boldsymbol{R}^{(i)}(\boldsymbol{\rho}, \boldsymbol{u}^i, \boldsymbol{u}^{i-1}, ..., \boldsymbol{u}^0) \right] \tag{21}$$

where $\boldsymbol{\rho}$ is the design variable and the variable $\boldsymbol{u}$ is the state variable (containing all the variables evaluated through forward analysis). Note that $\Theta = \theta$ since $R^{(i)} = 0$ for all

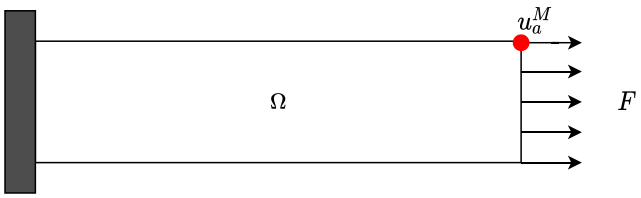

Fig. 5 Design domain for sensitivity calculations and its verification

i. Therefore, $\frac{d\Theta}{d\rho} = \frac{d\theta}{d\rho}$. Differentiating (21) with respect to the design variable $\boldsymbol{\rho}$, we obtain:

$$\frac{d\Theta}{d\boldsymbol{\rho}} = L^T \frac{d\boldsymbol{u}^M}{d\boldsymbol{\rho}} + \sum_{i=1}^{M} \left[\boldsymbol{\lambda}^{(i)T} \left(\sum_{k=1}^{i} \frac{\partial \boldsymbol{R}^{(i)}}{\partial \boldsymbol{u}^{(k)}} \frac{d\boldsymbol{u}^{(k)}}{d\boldsymbol{\rho}} + \frac{\partial \boldsymbol{R}^{(i)}}{\partial \boldsymbol{\rho}} \right) \right] \tag{22}$$

Expanding the right-hand side terms yields:

$$\begin{aligned} \frac{d\Theta}{d\boldsymbol{\rho}} = L^T \frac{d\boldsymbol{u}^M}{d\boldsymbol{\rho}} + \sum_{i=1}^{M} \boldsymbol{\lambda}^{(i)T} \frac{\partial \boldsymbol{R}^{(i)}}{\partial \boldsymbol{\rho}} + \boldsymbol{\lambda}^{(M)T} \left(\frac{\partial \boldsymbol{R}^{(M)}}{\partial \boldsymbol{u}^{(M)}} \frac{d\boldsymbol{u}^{(M)}}{d\boldsymbol{\rho}} \right) \\ + \sum_{i=1}^{M-1} \sum_{k=i}^{M} \left(\boldsymbol{\lambda}^{(k)T} \frac{\partial \boldsymbol{R}^{(k)}}{\partial \boldsymbol{u}^{(i)}} \right) \frac{d\boldsymbol{u}^{(i)}}{d\boldsymbol{\rho}} \end{aligned} \tag{23}$$

The solution of $\{\boldsymbol{\lambda}^i\}$ which causes all the implicit terms, $\{\frac{d\boldsymbol{u}}{d\boldsymbol{\rho}}\}$,[1] to vanish is given by:

$$\begin{aligned} \boldsymbol{\lambda}^{(M)} &= -L^T \left[\frac{\partial \boldsymbol{R}^{(M)}}{\partial \boldsymbol{u}^{(M)}} \right]^{-1} \\ \boldsymbol{\lambda}^{(i)} &= - \left[\sum_{k=i+1}^{M} \boldsymbol{\lambda}^{(k)T} \frac{\partial \boldsymbol{R}^{(k)}}{\partial \boldsymbol{u}^{(i)}} \right] \left[\frac{\partial \boldsymbol{R}^{(i)}}{\partial \boldsymbol{u}^{(i)}} \right]^{-1} \end{aligned} \tag{24}$$

When solved in this way, the parameters $\{\boldsymbol{\lambda}^i\}$ are referred to as the *adjoint* vectors, and each vector $\boldsymbol{\lambda}^{\boldsymbol{i}}$ represents the adjoint state at each time step t_i. Algorithm 1 contains a pseudocode description of the algorithm used to compute the sensitivities of the SMP material.

Algorithm 1 Time-dependent adjoint sensitivity analysis algorithm.

$\frac{df}{d\boldsymbol{\rho}} \leftarrow \frac{\partial}{d\boldsymbol{\rho}} \left[f(\boldsymbol{\rho}, \boldsymbol{u}^{(M)}) \right]$ /* initialize sensitivities */
$\boldsymbol{\lambda}^{(M)} \leftarrow \left[\frac{\partial \boldsymbol{R}^{(M)}}{\boldsymbol{u}^{(M)}} \right]^{-1} \left[-\frac{\partial f}{\boldsymbol{u}^{(M)}} \right]$ /* solve for final adjoint state */
for $i \leftarrow M, M-1, ..., 0$ **do**
  /* cycle back through each time step */
  $\boldsymbol{F}_{RHS} \leftarrow 0$;
  /* Cycle forward through all subsequent time steps */
  for $k \leftarrow i+1, i+2, M$ **do**
    $\frac{\partial \boldsymbol{R}^{(k)}}{\partial \boldsymbol{u}^{(i)}} \leftarrow \frac{\partial \boldsymbol{\varepsilon}^{ir}_{(k)}}{\partial \boldsymbol{\varepsilon}^{r}_{(i)}} + \frac{\partial \boldsymbol{\varepsilon}^{ig}_{(k)}}{\partial \boldsymbol{\varepsilon}^{r}_{(i)}} + \frac{\partial \boldsymbol{\varepsilon}^{i}_{(k)}}{\partial \boldsymbol{\varepsilon}^{r}_{(i)}} + \frac{\partial \boldsymbol{\varepsilon}^{is}_{(k)}}{\partial \boldsymbol{\varepsilon}^{r}_{(i)}}$;
    /* Each additive term is traced back in time through the recursive Algorithms 2 and 3 */
    $\boldsymbol{F}_{RHS} \leftarrow \boldsymbol{F}_{RHS} - \left[\boldsymbol{\lambda}^{(k)} \frac{\partial \boldsymbol{R}^{(k)}}{\partial \boldsymbol{u}^{(i)}} \right]$
  $\boldsymbol{\lambda}^{(i)} \leftarrow -\boldsymbol{F}_{RHS} \left[\frac{\partial \boldsymbol{R}^{(i)}}{\partial \boldsymbol{u}^{(i)}} \right]^{-1}$ /* solve for intermediate adjoint vectors (24) */
  $\frac{df}{d\boldsymbol{\rho}} \leftarrow \frac{\partial f}{\partial \boldsymbol{\rho}} + \boldsymbol{\lambda}^{(i)} \frac{\partial \boldsymbol{R}^{(i)}}{\partial \boldsymbol{\rho}}$

Once we obtain the full set of *adjoint* vectors, the sensitivities can be obtained as:

$$\frac{d\Theta}{d\boldsymbol{\rho}} = \sum_{i=0}^{M} \boldsymbol{\lambda}^i \frac{\partial \boldsymbol{R}^i}{\partial \boldsymbol{\rho}} \tag{25}$$

6 Numerical results

6.1 Self-actuating beam

The first case study discusses the design of an SMP-based self-actuating cantilever beam which, when subjected to a uniaxial load, exhibits a non-axial bending deformation. The initial design domain along with the boundary and loading conditions are shown in Fig. 6. The structure is fixed at one end while a constant uni-axial force (F) is applied at the other end while decreasing the temperature from T_H to T_L. The objective is to tailor the material distribution inside the design domain such that the displacement in y-direction at a particular node, ${U_y}^N$, is maximized at the end of the step III of the thermomechanical cycle when the domain is heated from T_L to T^*, while constraining the total amount of the SMP^1 material used. Mathematically, the optimization problem can be formulated as:

$$\begin{aligned} \underset{\boldsymbol{\rho}}{\text{minimize}} \quad & -{U_y}^N|_{t=T^*} \\ \text{subject to} \quad & V_{SMP^1}(\boldsymbol{\rho}) \leq V^{Max}_{SMP^1}, \quad 0 \leq \boldsymbol{\rho} \leq 1 \end{aligned} \tag{26}$$

[1] Note that implicit derivatives, $\frac{d*}{d\boldsymbol{\rho}}$, capture implicit dependence of a function or state variable with respect to ρ due to the solution of the residual, whereas explicit derivatives capture only direct dependence. Consequently, implicit derivatives are more expensive to evaluate, and therefore we seek to eliminate them from the sensitivity calculation

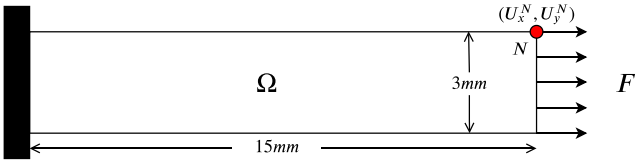

Fig. 6 Initial design domain with boundary conditions and loading conditions

Here, T^* represents the time at the end of step III. The term V_{SMP^1} represents the volume fraction of SMP material of type 1, represented by SMP^1, used by the algorithm. It is defined as:

$$V_{SMP^1} = \frac{\sum_{i=1}^{ne}(1-\rho_i)v^i}{\sum_{i=1}^{ne} v^i} \tag{27}$$

where the elemental design variable ρ_i is defined as:

$$\rho_i = \frac{v^i_{SMP^2}}{v^i} \tag{28}$$

where v^i is the total volume of an element. The term $V^{Max}_{SMP^1}$ is the maximum allowable volume fraction of SMP^1 material which is set to 0.7 in this implementation.

The design domain selected has a length of 15 mm, a height of 3 mm, and a thickness of 1 mm. The initial design domain is meshed with 120 × 24 linear quadrilateral elements. The SMP thermo-mechanical cycle is applied as described above. The optimized design is shown in Fig. 7 for a load of F = 0.01 N applied during step I. In the optimized design shown in Fig. 7, we can observe that the SMP^1 material with the lower glass-transition temperature is mostly concentrated along the upper surface of the beam while the SMP material with the higher glass-transition temperature is primarily distributed toward the base and the free edges the design domain. This can be explained by the fact that at the end of step III, as the temperature reaches T^*, the SMP^2 material has a considerably higher volume fraction of glass phase as compared to SMP^1, due to which the upper surface wants to retract back to its original length but this movement is restricted by the SMP^2 material resulting in an upward deflection of the structure as shown in Fig. 8.

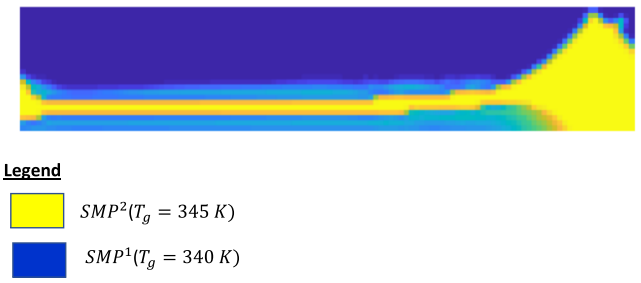

Fig. 7 Optimized material distribution for design of the beam

Keeping the optimized distribution of the two SMP materials the same inside the design domain, Fig. 8 shows the deformation of the structure due to different loading values applied during step I.

Figure 8 compares the maximum deflection of the self-actuating beam for different values of F applied during the step I of the thermo-mechanical programming cycle. The initial design domain is shown by the blue dashed lines in Fig. 8. The maximum displacement in the y-direction, $U_y{}^N$, for a value of F = 0.01 N, shown in Fig. 8a, is of magnitude 0.5567 mm. The initial design domain (shown with a dashed line) and the beam deformation corresponding to F = 0.05 N are shown in Fig. 8b for which the value of $U_y{}^N$ is 2.6531 mm (Fig. 9).

Figure 15 shows the finite element meshes at different stages of the applied thermo-mechanical cycle for F = 0.05 N. The beam design for a mesh size of 120 × 24 took over 64,627 core-hours on 144 processors and 340 optimization iterations to converge to the above design.

The optimization convergence history of the objective and constraint functions for the design of the self-actuating beam is shown in Fig. 10.

The result shown in Fig. 7 contains visible regions of intermediate material, whose properties are a combination of SMP^1 and SMP^2. Because the design problem does not prioritize stiffness, these regions are not deemed inefficient from the standpoint of the optimizer. Measures could be taken to suppress the presence of these regions (potentially sacrificing some degree of performance). However, we have not pursued these measures, since the intermediate materials do not hinder the manufacturability of the design. Indeed, current 3D printing technology for shape memory polymers allows us to generate *digital* hybrid materials, whose material properties are an interpolation of two baseline materials (Ge et al. 2014).

Figure 11 shows the optimized material distribution for the design of the self-actuating beam with penalization parameter $p = 1$. The maximum displacement in the positive y-direction, $U_y{}^N$, for a value of $F = 0.01$N is of magnitude 0.5276 mm. When we take the optimized material distribution obtained with $p = 3$ and run the forward analysis with $p = 1$, we obtain the value of $U_y{}^N$ as 0.5157 mm. Therefore, the $p = 1$ design is similar to the $p = 3$ design in both material distribution and displacement performance. The result indicates that for this problem, penalization is not necessary to achieve a binary solution. This can be explained by the fact that the optimizer naturally seeks a design in which the transition temperatures of the two material regions are as far apart as possible in order to maximize the disparity in strain response at the end of stage III of the thermo-mechanical programming cycle. This will lead to the largest tip deflection.

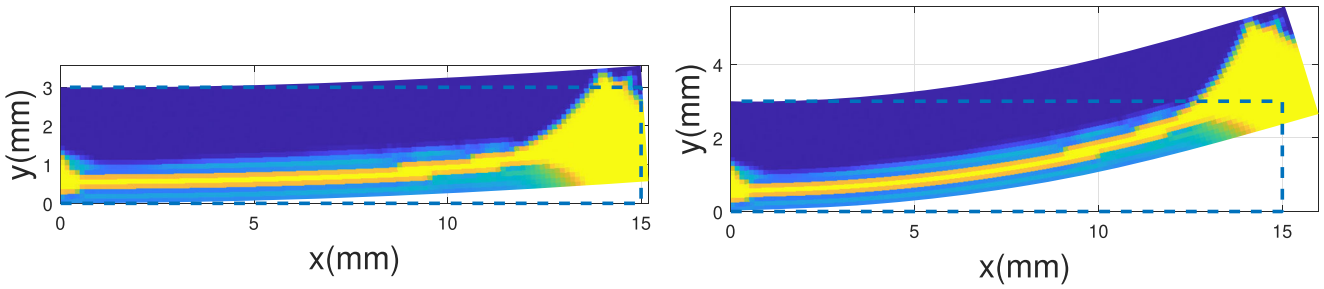

(a) F = 0.01 N **(b)** F = 0.05 N

Fig. 8 Maximum bending deflection for different amounts of uniaxial stretching during the thermo-mechanical programming cycle

To compare the performances of the optimized structure under the influence of the reduced and full thermo-mechanical cycle, the optimized structure shown in Fig. 11 was analyzed subject to the full thermo-mechanical cycle. To simulate comparable loading and cooling conditions, the optimized structure was subjected to a constant load of $F = 0.01\ N$ at temperature T_H for a total time of 20 min simulated with 4 time steps. Then it was allowed to relax, while the external deformation was held constant, for a time of 10 min simulated with 2 time steps. Holding the external deformations constant, the temperature was decreased from T_H to T_L over a time of 20 min simulated with 4 time steps. Then, the structure was allowed to relax without any external constraints for a total time of 15 min simulated with 3 time steps. This was followed by increasing the temperature from T_L to T^* over a duration of 10 min. The tip deflection was found to be 0.5686 mm. The 7.7% increase in the tip deflection can be attributed to the fact that the structure was subjected to loading at higher temperatures for longer duration due to which it stretched more during the deformation stage. This led to the slight increase in the final tip deflection measured at the end of the heating step.

Figure 12 shows the optimized self-actuating beam for different initial starting points with $p = 1$. Here, three additional starting points have been explored. Figure 12b shows the optimized material distribution for a random initialization of the design variable. The value of ${U_y}^N$ is 0.5301 mm in the positive y-direction. Figure 12d shows the optimized material distribution for an informed guess with the upper-half of the beam initialized to $\rho = 0$ and the lower-half of the beam initialized to $\rho = 1$. The value of ${U_y}^N$ is 0.5303 mm in the positive y-direction for this case. Figure 12f shows the optimized material distribution for an uniform initial guess with $\boldsymbol{\rho} = 1.0$. The final value of ${U_y}^N$

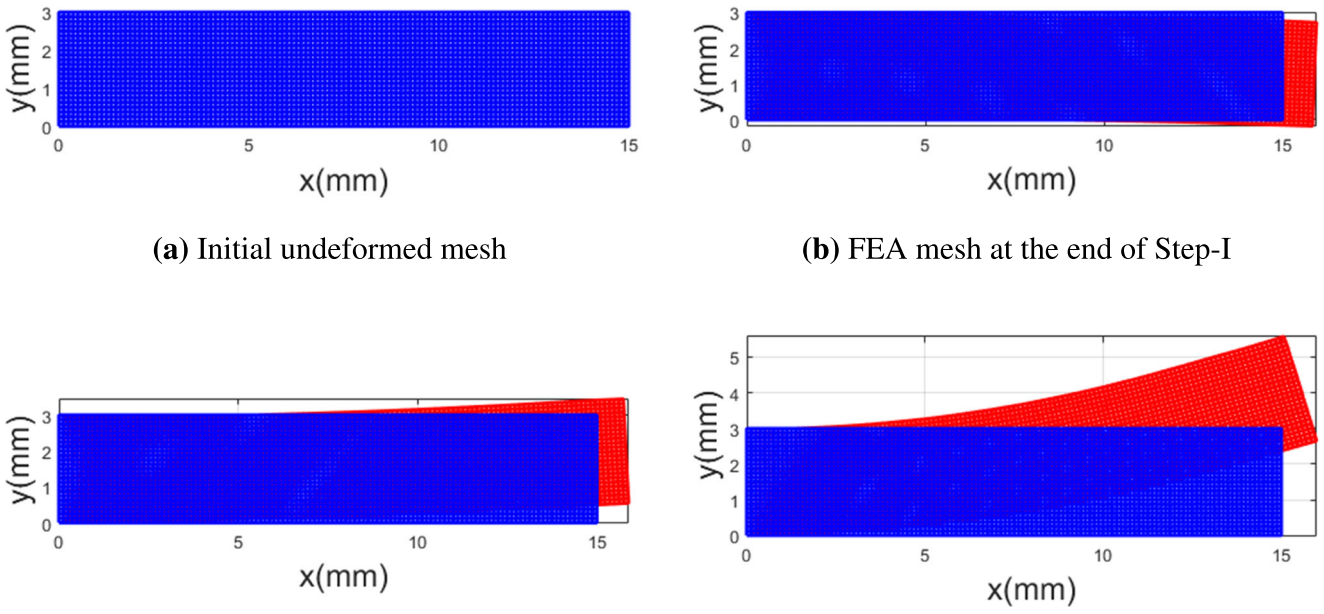

(a) Initial undeformed mesh **(b)** FEA mesh at the end of Step-I

(c) FEA mesh at the end of Step-II **(d)** FEA mesh at the end of Step-III

Fig. 9 Finite element meshes of the self-actuating beam at each stage of the condensed thermo-mechanical programming cycle for $F = 0.05$ N

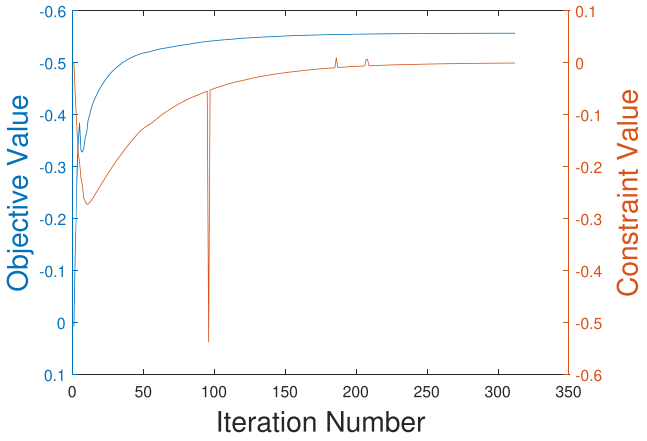

Fig. 10 Convergence history of the objective and constraint functions for the self-actuating beam optimization

is 0.5291 mm. We observe that in all of these cases, the material distribution converges to a pattern similar to that obtained using a *neutral* starting point in which all elements have the same initial material fraction. The results suggest that the conventional approach of using a *neutral* starting point yields satisfactory results.

6.2 Self-actuating gripper (SAG) design

The second case study discusses the design of an SMP-based self-actuating gripper. The loading and boundary conditions are shown in Fig. 13. The optimization problem statement is similar to that of the self-actuating beam design problem with the displacement ${U_y}^N$ in the downward direction. Here, we have used the symmetry of the design domain to optimize the distribution of material only on the top-half. This reduces the computational cost by reducing the effective size of the mesh; as a result, only the displacement of a single node (marked with a red dot) is used for the optimization problem formulation.The design domain has dimensions 100 mm × 100 mm and is meshed with 7200 equally sized 4-node square elements. The square-shaped cutout has dimensions of 25 mm×25 mm. The force (F) applied during step I is 0.017 N. The whole structure is subjected to the SMP-modified thermo-mechanical cycle, and the goal of the topology optimization algorithm is to maximize the displacement at the end of step III. The idea behind maximizing the displacement is to achieve a gripping motion.

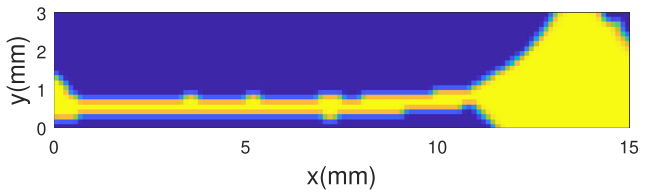

Fig. 11 Optimized material distribution with penalization parameter $p = 1$

Figure 14 shows the optimized distribution of the two SMP materials inside the design domain with maximized tip displacement of the gripper (Fig 15). Figure 16 shows the deformed SAG configuration superimposed on the original undeformed shape shown by the red dashed lines. The optimized value of ${U_y}^N$ obtained with a loading of 0.017 N is 2.3472 mm, in the negative y-direction. As explained in Section 6.1, a higher quantity of the SMP^1 material, with lower glass-transition temperature, is concentrated near the node N, interspersed with the SMP^2 material, having the higher glass-transition temperature. As the temperature reached T^*, at the end of the step III, the SMP^1 material tries to contract due to the conversion of glass phase to rubber phase inside the material. This contraction is resisted by the finger-like regions, consisting of SMP^2, which still has a predominant glass phase. This strain imbalance leads to the bending of the jaws, giving rise to the gripping action. The SAG design for a mesh size of 120 × 60 took over 215,136 core-hours on 144 processors and 498 optimization iterations to generate the above design.

The optimization convergence history of the objective and constraint functions for the design of the self-actuating gripper is shown in Fig. 17.

6.3 Design of a 3D torsional structure

To expand the current framework to design 3D structures, we have applied the above-described methodology to the design of a torsional unit structure. The unit structure will exhibit torsion about the axis along which the unit is stretched during the programming cycle. The design domain for the structure is shown in Fig. 18. It has dimensions of 100 mm×20 mm×20 mm and is discretized with 25 ×5× 5, 8 node cubic elements. The design domain is fixed at one end while a force (F) of 0.05 N is applied during the thermo-mechanical programming cycle as shown in Fig. 18.

The objective is to tailor the material distribution inside the design domain such that the displacement in z-direction at the degree-of-freedom, ${U_z^2}^N$, is minimized at the end of the step III of the thermo-mechanical cycle, while constraining the U_z^1 d.o.f to be in the positive z-direction, greater than a certain baseline value U_0, also evaluated at the end of step III. The total amount of SMP^1 material used is also constrained to a maximum limit of $V_{SMP^1}^{max}$. Mathematically, the optimization problem can be formulated as:

$$\begin{aligned} \underset{\boldsymbol{\rho}}{\text{minimize}} \quad & U_z^2|_{t=T^*} \\ \text{subject to} \quad & V_{SMP^1}(\boldsymbol{\rho}) \leq V_{SMP^1}^{Max}, \quad 0 \leq \boldsymbol{\rho} \leq 1 \\ & U_z^1|_{t=T^*} > U_0 \end{aligned} \tag{29}$$

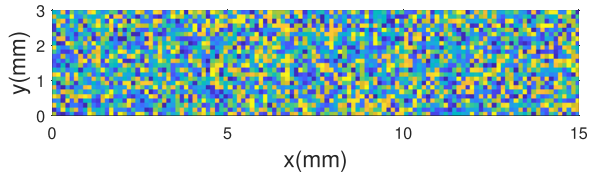

(a) Initial random distribution of design variable

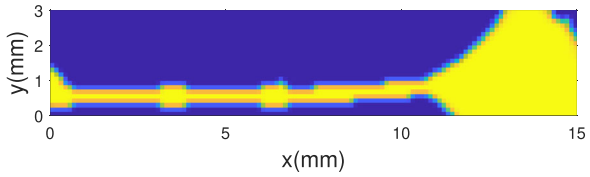

(b) optimal material distribution

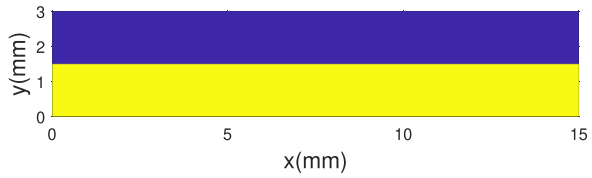

(c) Informed guess for distribution of design variable

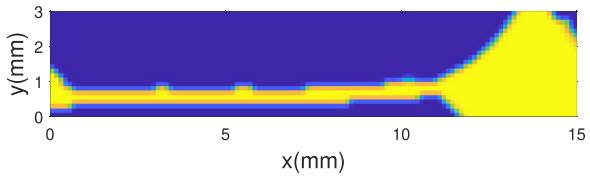

(d) optimal material distribution

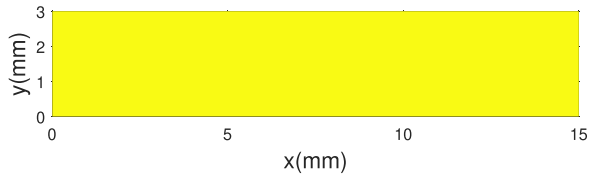

(e) Initial domain with $\boldsymbol{\rho} = 1.0$

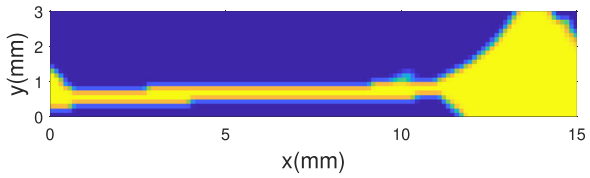

(f) optimal material distribution

Fig. 12 Optimized material distribution for different initial conditions

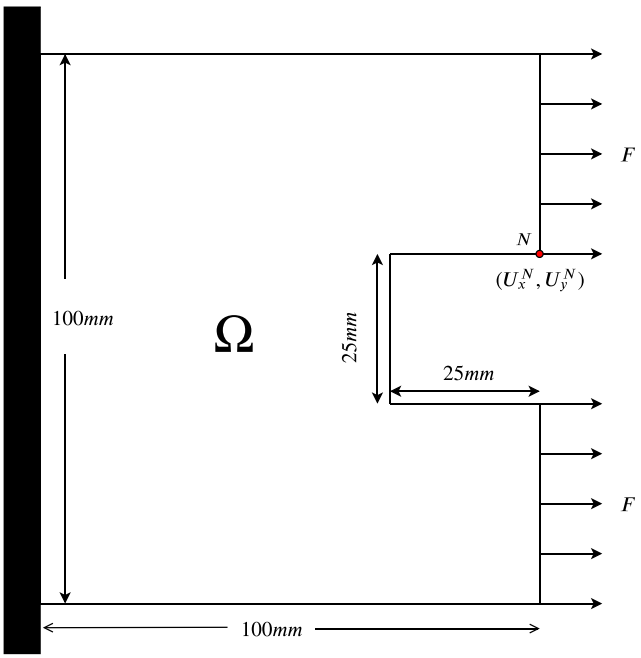

Fig. 13 Initial design domain of the self-actuating gripper with boundary conditions and loading conditions

The constant U_0 is evaluated as:

$$U_0 = 0.8(U_z^1)_{initial} \tag{30}$$

where $(U_z^1)_{initial}$ refers to the U_z^1 for the initial design domain corresponding to the application a uniaxial force before the start of the optimization. Figure 19 shows the optimized material distribution for the 3D torsional structure design problem. For a force of $F = 0.05\ N$,

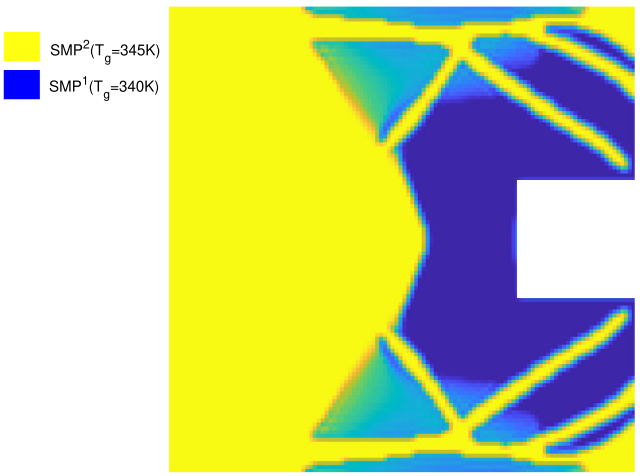

Fig. 14 Optimized material distribution for the self-actuating gripper design

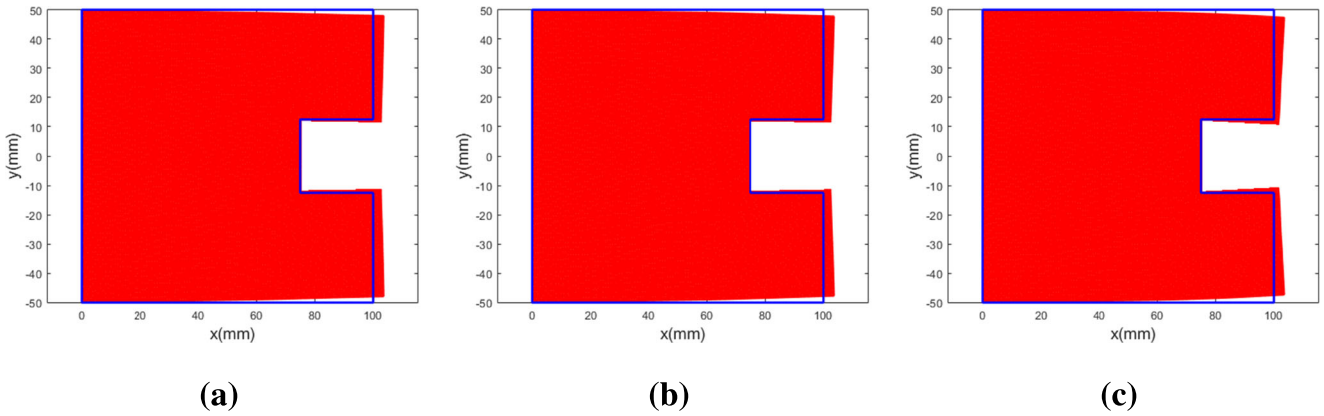

Fig. 15 Self-actuating gripper mesh at different stages of the condensed thermo-mechanical programming cycle. **a** Deformed mesh at the end of the step I. **b** Deformed mesh at the end of step II. **c** Mesh at the end of step III

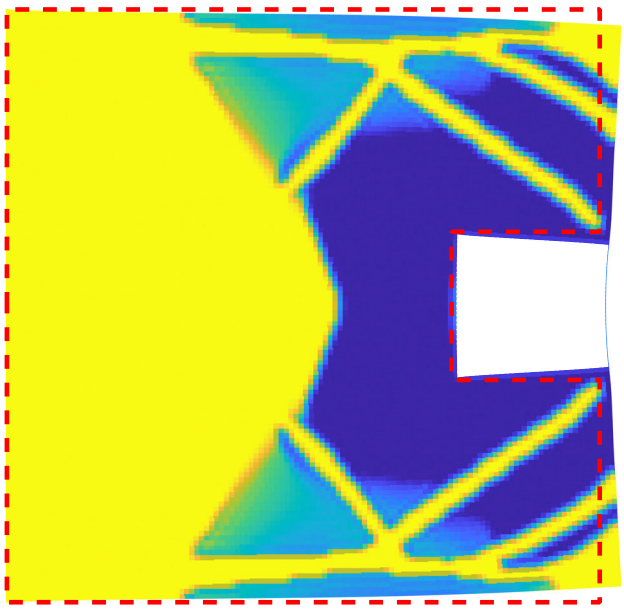

Fig. 16 Comparison of the SAG in the deformed configuration with the original undeformed domain (dashed red line)

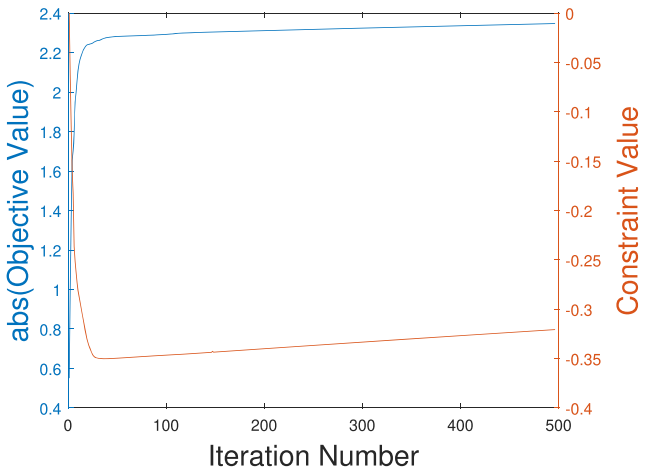

Fig. 17 Convergence history of the objective and constraint functions for the self-actuating gripper optimization

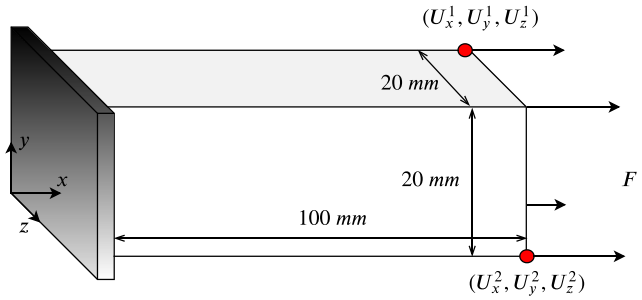

Fig. 18 Design domain and boundary conditions for the 3D torsional unit structure

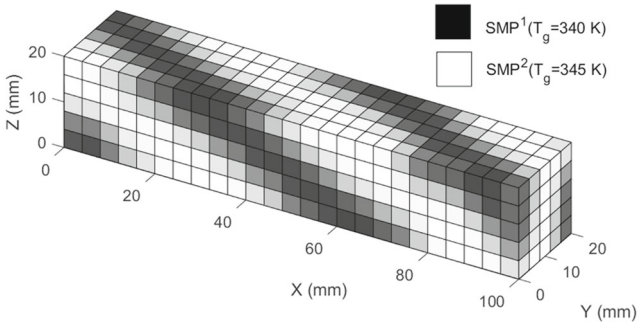

Fig. 19 Optimized material distribution for 3D torsional structure

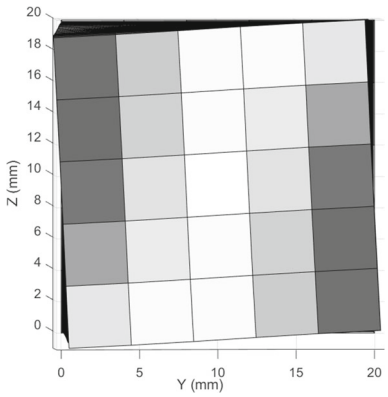

Fig. 20 The 3D torsional structure after deformation due to shape memory response (view from the free face at $x = 100$ mm)

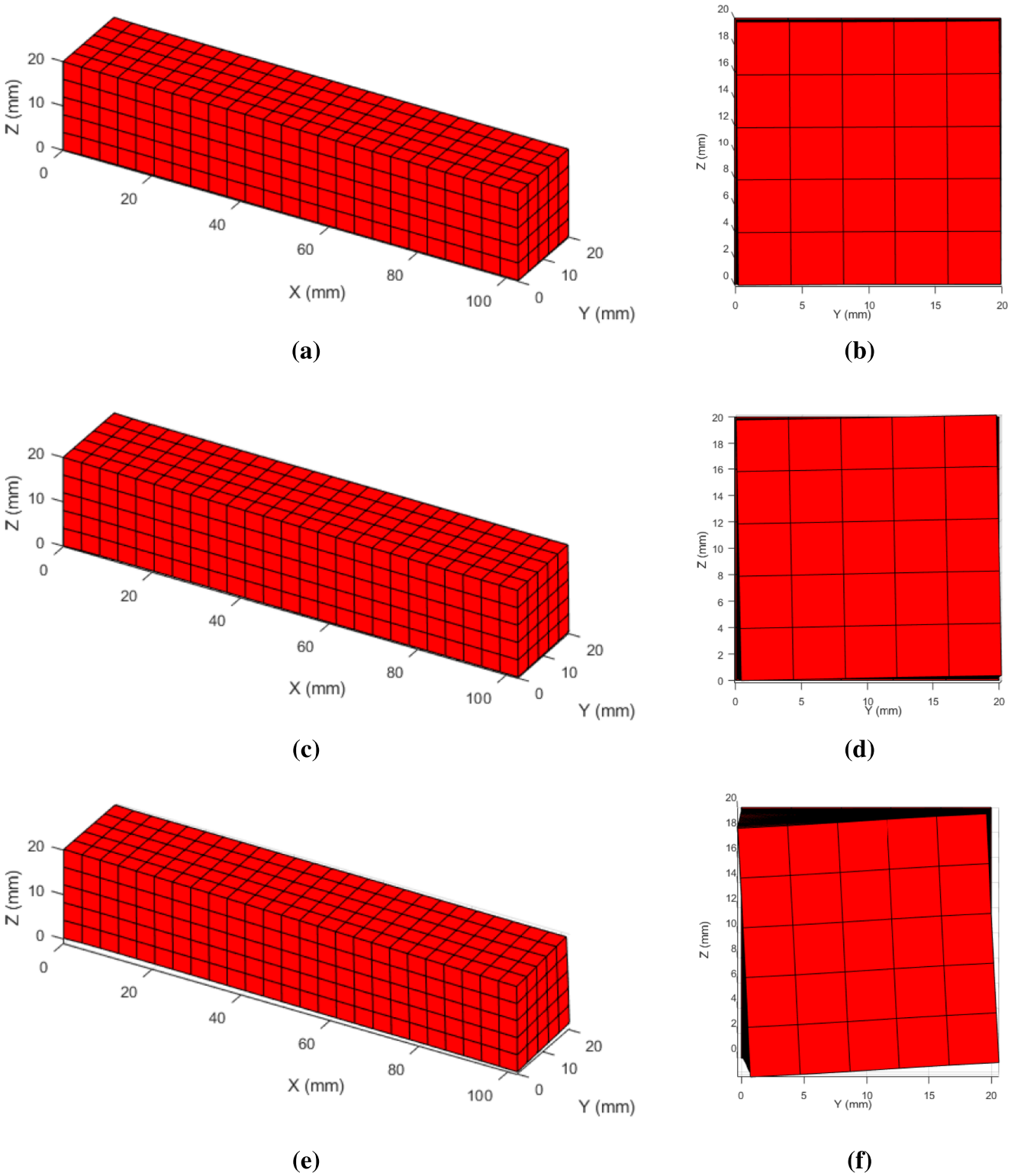

Fig. 21 3D optimized torsional structure at different stages of the modified thermo-mechanical cycle. **a**, **b** Isometric and front views of the deformed mesh at the end of step I. **c**, **d** Isometric and front views of the deformed mesh at the end of step II. **e**, **f** Twisted mesh at the end of step III of the modified thermo-mechanical cycle

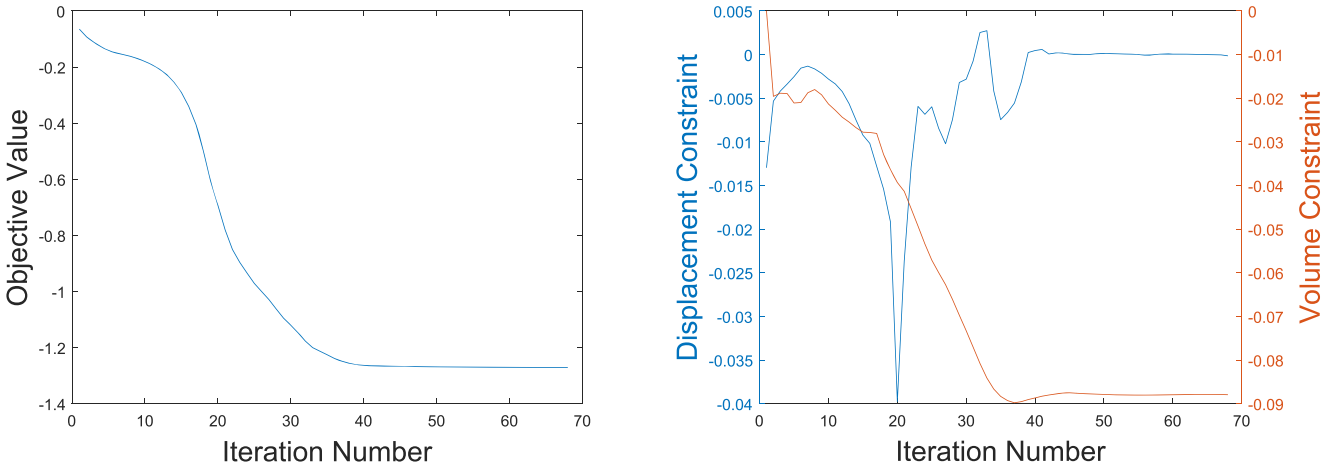

Fig. 22 Optimization convergence history for the 3D torsional structure optimization

the displacements of U_z^2 and U_z^1 are -1.2710 mm and 0.5985 mm respectively.

We can observe from Fig. 19 that the SMP^1 and SMP^2 materials are arranged as bands, running diagonally across the structure, very similar to the helical and spiral structural arrangements found in natural twisted structures.

Figure 20 shows twisting of the structure achieved through optimal distribution of SMP materials with simple axial stretching of the structure applied during the programming cycle.

The deformation of the structural mesh at different stages of the modified thermo-mechanical cycle of the 3D torsional structure for the optimized material layout is shown in Fig. 21. The convergence history of the objective function and the constraints for the design of the 3D torsional structure is shown in Fig. 22.

Figure 23 shows the optimized design domain with the penalization constant $p = 1$. For a force of $F = 0.05\ N$, the displacements of U_z^2 and U_z^1 are -1.2024 mm and

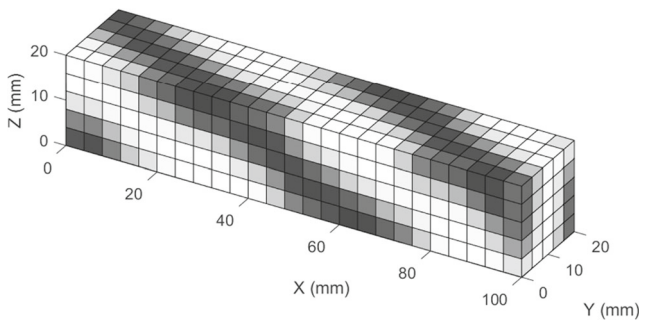

Fig. 23 Optimized material distribution for 3D torsional structure with $p = 1$

0.4868 mm respectively. When we take the final optimized material distribution for $p = 3$ and run the forward analysis with $p = 1$, we obtain the value of the displacements U_z^2 and U_z^1 as -1.1956 mm and 0.0554 mm respectively. We observe that the absolute value of U_z^2 increases from 1.1956 mm for $p = 3$ to 1.2024 mm for $p = 1$.

7 Conclusion

A novel framework for computationally designing multimaterial active structures containing SMPs was implemented to optimally exploit the material's shape memory characteristics. The constitutive modelling of SMPs proposed by Baghani et al. (2012) was implemented on a finite-element framework using the PETSc library to simulate SMP behavior over the thermo-mechanical cycle. The structural deformations and the thermally activated shape memory response were analyzed using a small-strain, multi-phase FEA model. The gradient information required for topology optimization was calculated using a time-dependent adjoint sensitivity analysis. A recursive algorithm for sensitivity analysis, necessary for accurately capturing the path-dependent characteristics of the SMPs, was introduced and the details of its implementation have been provided. A novel condensed SMP thermo-mechanical programming cycle has been proposed to significantly reduce the computational cost involved in the analysis of the SMPs, while preserving the essential SMP characteristics. A fully parallel PETSc-based framework for topology optimization with multiple SMP materials was developed and implemented to well-refined multi-functional, multimaterial SMP structures. Three numerical results showcasing the application

of the current framework have been provided. Topology optimization was implemented to design a morphing beam capable of deforming in a non-axial direction with simple axial loading applied during the thermo-mechanical programming cycle. Design of a self-actuating gripper was also implemented. To further expand the scope of the current framework, a 3D torsional structure was designed capable of twisting about the axis along which it is stretched during the thermo-mechanical programming cycle. The results show that topology optimization can be successfully implemented to tailor the distribution of SMP materials in the undeformed domain so that when actuated using an external thermal stimulus, the structures exhibit different morphologies while fulfilling the required objectives. This research contributes to bridging the gap between computational design, and 4D printing. Future work will focus on design and 4D printing of multimaterial mechanisms with complex motion, including large deformations.

Funding The authors received financial support of the National Science Foundation under grant # CMMI-1663566.

Compliance with ethical standards

Conflict of interest The authors declare that they have no conflict of interest.

Replication of results Detailed descriptions of the algorithms used to generate all results are provided throughout the paper. Additionally, we have included all relevant material properties, and all algorithm parameters. Copies of the code used to generate the results will be made available upon request.

Appendix 1: Finite element derivations

The subscript, n, represents the time step.

The terms $\mathbb{A}_r$, $\mathbb{A}_g$, $\mathbb{H}_r$, $\mathbb{H}_g$, $\mathbb{B}_r$, $\mathbb{B}_g$, and $\Delta\phi^g_{n+1}$ required in (A.2) are computed as:

$$\begin{aligned}
\mathbb{A}_r &= (\mathbb{K}^r_{neq} + \mathbb{K}^r_{eq}) - \frac{\Delta t}{\eta_r}\mathbb{K}^r_{neq}\mathbb{H}^{r\,-1}\mathbb{K}^r_{neq}\\
\mathbb{A}_g &= (\mathbb{K}^g_{neq} + \mathbb{K}^g_{eq}) - \frac{\Delta t}{\eta_g}\mathbb{K}^g_{neq}\mathbb{H}^{g\,-1}\mathbb{K}^g_{neq}\\
\mathbb{H}_r &= \mathbb{I} + \frac{\Delta t}{\eta_r}\mathbb{K}^r_{neq}\\
\mathbb{H}_g &= \mathbb{I} + \frac{\Delta t}{\eta_g}\mathbb{K}^g_{neq}\\
\mathbb{B}_r &= \mathbb{H}_r^{-1}\mathbb{K}^r_{neq}\\
\mathbb{B}_g &= \mathbb{H}_g^{-1}\mathbb{K}^g_{neq}\\
\Delta\phi^g_{n+1} &= \phi^g_{n+1} - \phi^g_n
\end{aligned} \tag{A.1}$$

The terms $\mathbb{W}_r$, $\mathbb{W}_g$, $\mathbb{M}$, $\mathbb{N}$, $\mathbb{P}$, $\mathbb{O}$, $\mathbb{E}$, and $\mathbb{F}$ for (9) are defined as:

$$\begin{aligned}
\mathbb{W}_r &= \mathbb{H}_r^{-1}\left[\frac{\Delta t}{\eta_r}\mathbb{K}^r_{neq}\right]\\
\mathbb{W}_g &= \mathbb{H}_g^{-1}\left[\frac{\Delta t}{\eta_g}\mathbb{K}^g_{neq}\right]\\
\mathbb{M} &= \frac{\Delta t}{\eta_i}\mathbb{A}_r\\
\mathbb{N} &= \frac{\Delta t}{\eta_i}\mathbb{B}_r\\
\mathbb{P} &= \Delta\phi^g_{n+1}\\
\mathbb{O} &= \mathbb{A}_g^{-1}\mathbb{A}_r\\
\mathbb{E} &= -\mathbb{A}_g^{-1}\mathbb{B}_r\\
\mathbb{F} &= v\mathbb{A}_g^{-1}\mathbb{B}_g
\end{aligned} \tag{A.2}$$

Here, $\mathbb{I}$ is the fourth-order identity tensor given by:

$$\begin{aligned}
\mathbb{I}_{ijkl} &= \delta_{ik}\delta_{jl}\\
\delta_{ij} &= \begin{cases} 1, & \text{if } i = j,\\ 0, & \text{if } i \neq j. \end{cases}
\end{aligned} \tag{A.3}$$

Here, δ_{ij} is the Kronecker delta. Isotropic linear elastic constitutive law is utilized to compute the fourth-order elasticity tensors $\mathbb{K}^r_{eq}$ and $\mathbb{K}^r_{neq}$ corresponding to the rubbery-phase and $\mathbb{K}^g_{eq}$ and $\mathbb{K}^g_{neq}$ for the glassy-phase material.

Appendix 2: Derivation of sensitivity analysis

Having discussed the generalized formulation for time-dependent adjoint sensitivity analysis in Section 5, we focus on deriving the sensitivity formulation specifically for shape memory polymers. To avoid confusion in the notation representing inelastic strain components and time steps, from here on the current time step will be denoted by subscript $\{n+1\}$, the previous time step will be denoted by subscript $\{n\}$, and so on.

The sensitivity of the objective function is calculated via (25). This equation has two components: the first is the *adjoint* vectors ($\boldsymbol{\lambda}$) and the other is the component capturing the explicit dependence of the residual term on the design variable. The *adjoint* vectors are computed via (24). Evaluation of both of these components requires the residual

term ($\boldsymbol{R}$). The residual equation for the SMP can be stated as:

$$\begin{aligned}\boldsymbol{R}_{n+1} &= \int_\Omega \boldsymbol{B}^T \mathbb{A}^{(r)} \mathbb{D}_{n+1}^{-1} : \boldsymbol{B}\boldsymbol{u}_{n+1} dv - \int_\Omega \boldsymbol{B}^T \mathbb{X}_{n+1}^{(r)} : \boldsymbol{\varepsilon}_n^{(ir)} dv \\ &+ \int_\Omega \boldsymbol{B}^T \mathbb{X}_{n+1}^{(g)} : \boldsymbol{\varepsilon}_n^{(ig)} dv + \int_\Omega \boldsymbol{B}^T \mathbb{Y}_{n+1}^{(r)} : \boldsymbol{\varepsilon}_n^{(ir)} dv \\ &- \int_\Omega \boldsymbol{B}^T \mathbb{V}_{n+1} : \boldsymbol{\varepsilon}_n^{(i)} dv - \int_\Omega \boldsymbol{B}^T \mathbb{Z}_{n+1}^{(r)} : \boldsymbol{\varepsilon}_n^{(is)} dv \\ &- \int_\Omega \boldsymbol{B}^T \mathbb{A}^{(r)} \mathbb{D}_{n+1}^{-1} : \boldsymbol{\varepsilon}_{n+1}^{Th} dv - \boldsymbol{F}^{ext} \end{aligned} \tag{B.1}$$

where the terms $\mathbb{X}_{n+1}^{(r)}$, $\mathbb{X}_{n+1}^{(g)}$, $\mathbb{Y}_{n+1}^{(r)}$, $\mathbb{V}_{n+1}^{(r)}$, $\mathbb{Z}_{n+1}^{(r)}$ are given by:

$$\begin{aligned}\mathbb{X}_{n+1}^{(r)} &= \mathbb{A}_r \mathbb{D}_{n+1}^{-1} \phi_{n+1}^{(g)} {\mathbb{A}_g}^{-1} \mathbb{B}_r \\ \mathbb{X}_{n+1}^{(g)} &= \mathbb{A}_r \mathbb{D}_{n+1}^{-1} \phi_{n+1}^{(g)} {\mathbb{A}_g}^{-1} \mathbb{B}_g \\ \mathbb{Y}_{n+1}^{(r)} &= \mathbb{A}_r \mathbb{D}_{n+1}^{-1} \left(\frac{\Delta t}{\eta_i}\right) \mathbb{B}_r \\ \mathbb{V}_{n+1}^{(r)} &= \mathbb{A}_r \mathbb{D}_{n+1}^{-1} \\ \mathbb{Z}_{n+1}^{(r)} &= \mathbb{A}_r \mathbb{D}_{n+1}^{-1} \end{aligned} \tag{B.2}$$

The differentiation of the residual equation, $\boldsymbol{R}_{n+1}$, with respect to the design variables can be computed by:

$$\begin{aligned}\frac{\partial \boldsymbol{R}_{n+1}}{\partial \boldsymbol{\rho}} &= \int_\Omega \boldsymbol{B} \frac{\partial \boldsymbol{\sigma}_{n+1}}{\partial \boldsymbol{\rho}} dv - \frac{\partial \boldsymbol{F}_{n+1}^{ext}}{\partial \boldsymbol{\rho}} \\ \frac{\partial \sigma_{n+1}}{\partial \boldsymbol{\rho}} &= \frac{\partial \mathbb{A}_r}{\partial \rho} : \boldsymbol{\varepsilon}_{n+1}^{(r)} + \mathbb{A}_r : \frac{\partial \boldsymbol{\varepsilon}_{n+1}^{(r)}}{\partial \boldsymbol{\rho}} - \frac{\partial \mathbb{B}_r}{\partial \boldsymbol{\rho}} : \boldsymbol{\varepsilon}_n^{(ir)} - \mathbb{B}_r : \frac{\partial \boldsymbol{\varepsilon}_n^{(ir)}}{\partial \boldsymbol{\rho}} \end{aligned} \tag{B.3}$$

To evaluate the *adjoint* vectors, it is required to capture the explicit dependence of the residual for the k^{th} time step on the displacement of the i^{th} time step, i.e., $\frac{\partial \boldsymbol{R}_k}{\partial \boldsymbol{u}_i}$. These terms are referred to as the "coupling" terms. Finding the $\frac{\partial \boldsymbol{R}_k}{\partial \boldsymbol{u}_i}$ terms are more involved since at each time step there is an exponential growth of terms from the previous time step.

For example, let us evaluate the term $\frac{\partial \boldsymbol{R}_{n+1}}{\partial \boldsymbol{u}_{n-1}}$. The coupling term $\frac{\partial \boldsymbol{R}_{n+1}}{\partial \boldsymbol{u}_{n-1}}$ is proportional to $\frac{\partial \boldsymbol{R}_{n+1}}{\partial \boldsymbol{\varepsilon}_{n-1}}$, since strain is a linear function of displacement (u). We can use the chain rule to write:

$$\frac{\partial \boldsymbol{R}_{n+1}}{\partial \boldsymbol{u}_{n-1}} \propto \frac{\partial \boldsymbol{R}_{n+1}}{\partial \boldsymbol{\varepsilon}_{n-1}} \approx \underbrace{\frac{\partial \boldsymbol{R}_{n+1}}{\partial \boldsymbol{\varepsilon}_{n-1}^{(r)}}}_{\text{term I}} \overbrace{\frac{\partial \boldsymbol{\varepsilon}_{n-1}^{(r)}}{\partial \boldsymbol{\varepsilon}_{n-1}}}^{\text{term II}} \tag{B.4}$$

Equation (B.4) gets contributions from *term I* and *term II*. The parameter $\boldsymbol{R}_{n+1}$ which represents the residual, obtained during the forward analysis, is given by (B.1) which has seven terms. Each of the terms, at a particular time step, is dependent not only on the current time step of the evaluation but also on the previous time step as shown in (9). For example, if we calculate the coupling coefficients from the second term, $\int_\Omega \boldsymbol{B}^T \mathbb{X}_{n+1}^{(r)} \boldsymbol{\varepsilon}_n^{(ir)} dv$, of the residual equation, and track the evolution of the term in time, we will get the map as shown in Fig. 24. The coefficient C_f is defined as:

$$C_f = \boldsymbol{B}^T \mathbb{X}_{n+1}^{(r)}$$

The terms $\mathbb{A}_n$ and $\mathbb{B}_n$ are given by:

$$\begin{aligned}\mathbb{A}_n &= \mathbb{D}_n^{-1} \left[-\phi_n^g \mathbb{A}_g^{-1} \mathbb{B}_r + \frac{\Delta t}{\eta_i} \mathbb{B}_r \right] \\ \mathbb{B}_n &= \mathbb{D}_n^{-1} \left[\phi_n^g \mathbb{A}_g^{-1} \mathbb{B}_g \right] \end{aligned}$$

If we collect the terms to evaluate $\frac{\partial \boldsymbol{\varepsilon}_n^{(ir)}}{\partial \boldsymbol{\varepsilon}_{n-1}^{(r)}}$, we get:

$$\begin{aligned}\frac{\partial \boldsymbol{\varepsilon}_n^{(ir)}}{\partial \boldsymbol{\varepsilon}_{n-1}^{(r)}} &= \Big[\mathbb{H}_r^{-1} \mathbb{W}_r + \mathbb{W}_r \mathbb{A}_n \mathbb{W}_r + \mathbb{W}_r \mathbb{B}_n \mathbb{W}_g \mathbb{O} \\ &+ \mathbb{W}_r \mathbb{D}_n^{-1} \mathbb{M} + \mathbb{W}_r \mathbb{D}_n^{-1} \mathbb{P} \Big] \end{aligned} \tag{B.5}$$

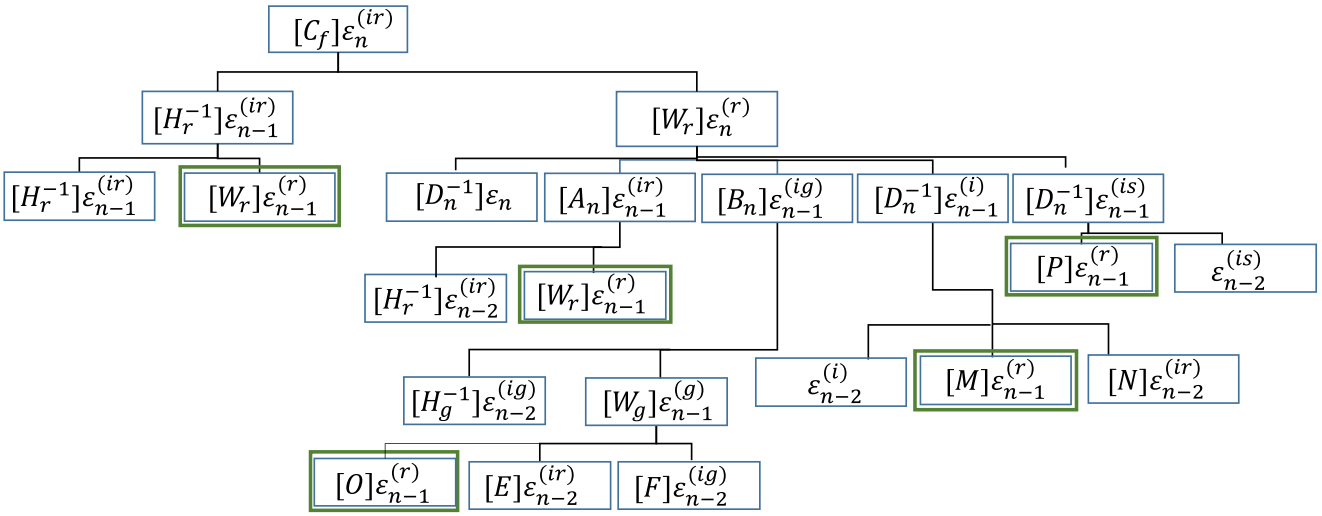

Fig. 24 Tracking $\frac{\partial \boldsymbol{\varepsilon}_n^{(ir)}}{\partial \boldsymbol{\varepsilon}_{n-1}^{(r)}}$ terms in time

Equation (B.5) represents *term I* in terms of $\varepsilon_n^{(ir)}$. A similar procedure is adopted for all the other six terms present in the (B.1) to make a total of twenty-three terms for the coupling term $\frac{\partial \boldsymbol{R}_{n+1}}{\partial \boldsymbol{u}_{n-1}}$. The computation of *term II* is straightforward and is given by:

$$\frac{\partial \boldsymbol{\varepsilon}_{n-1}^{(r)}}{\partial \boldsymbol{\varepsilon}_{n-1}} = \mathbb{D}_{n-1}^{-1} \tag{B.6}$$

Capturing the evolution of all the components required to accurately calculate the sensitivities makes this process computationally expensive and a highly time-consuming procedure. The time taken increases exponentially with the total number of time steps required to simulate the thermo-mechanical cycle of the SMP increases. The function and the recursive algorithm used to compute the $\{\frac{\partial R_k}{\partial u_i}\}$ terms for the total sensitivity analysis are shown in Algorithms 2 and 3. Note that for the recursive algorithm shown in Algorithm 3, parameters k and i represent the time steps. Here, the functions `func_eir`, `func_eig`, `func_is`, and `func_i` are programmable versions of $\boldsymbol{\varepsilon}^{(ir)}$, $\boldsymbol{\varepsilon}^{(ig)}$, $\boldsymbol{\varepsilon}^{(is)}$, and $\boldsymbol{\varepsilon}^{(i)}$, shown in (9), implemented for the k^{th} step. The variable $[M]$ is a collection of parameters representing the intrinsic material properties. The function f represents a general function manipulating its inputs and giving a desired output.

Algorithm 2 Psuedocode to calculate the terms $\frac{\partial R_k}{\partial u_i}$ for the sensitivity evaluation.

`sens_partI`(k, i, M)
$C_f = f(M)$ /* compute external variable C_f as a function of M */
/* call individual recursive functions */
$\frac{\partial \varepsilon_k^{(ir)}}{\partial \varepsilon_i^{(r)}} \leftarrow$ `func_eir`(C_f, k, i, M)
$\frac{\partial \varepsilon_k^{(ig)}}{\partial \varepsilon_i^{(r)}} \leftarrow$ `func_eig`(C_f, k, i, M)
$\frac{\partial \varepsilon_k^{(is)}}{\partial \varepsilon_i^{(r)}} \leftarrow$ `func_is`(C_f, k, i, M)
$\frac{\partial \varepsilon_k^{(i)}}{\partial \varepsilon_i^{(r)}} \leftarrow$ `func_i`(C_f, k, i, M);
term I $= f\left(\frac{\partial \varepsilon_k^{(ir)}}{\partial \varepsilon_i^{(r)}}, \frac{\partial \varepsilon_k^{(ig)}}{\partial \varepsilon_i^{(r)}}, \frac{\partial \varepsilon_k^{(is)}}{\partial \varepsilon_i^{(r)}}, \frac{\partial \varepsilon_k^{(i)}}{\partial \varepsilon_i^{(r)}}\right)$ /* term I of (B.4) is calculated using the output of the individual recursive functions */
term II $= f\left(\frac{\partial \varepsilon_i^{(r)}}{\partial \varepsilon_i}\right)$ /* term II of (B.4) is calculated */
Return: $\frac{\partial R_k}{\partial u_i} \leftarrow f$(term I, term II)

The individual functions have similar structures and one such function `func_eir` has been shown in details in Algorithm 3.

Algorithm 3 Recursive algorithm to capture strain evolution with time for the sensitivity evaluation.

`func_eir`(C_f, k, i, M)
$CI = \mathbb{H}_r^{-1}$ /* compute internal variable CI */
$\frac{\partial \varepsilon_k^{(r)}}{\partial \varepsilon_i^{(r)}} \leftarrow$ `func_er`(CI, k, i, M) /* call function which tracks evolution of strain variables as shown in (B.5) */
if $k > i$ **then**
$\frac{\partial \varepsilon_{k-1}^{(ir)}}{\partial \varepsilon_i^{(r)}} \leftarrow$ `func_eir`$(C_f \times CI, k-1, i, M)$ /* call itself with $k = k-1$ */
Return: $\frac{\partial \varepsilon_k^{(r)}}{\partial \varepsilon_i^{(r)}} + \frac{\partial \varepsilon_{k-1}^{(ir)}}{\partial \varepsilon_i^{(r)}}$ /* output */

To verify the implementation of the sensitivity analysis, the design domain shown in Fig. 5 is discretized with a coarse mesh of 45 elements. The structure is initialized with a uniform distribution of design variable $\boldsymbol{\rho} = 0.3$. It was then subjected to an axial stretching load $\boldsymbol{F} = 0.025\ N$ during the cooling phase of the thermo-mechanical cycle. The load was removed during the relaxation and heating phases of the thermo-mechanical programming cycle. The function of interest is the tip displacement $\boldsymbol{u}_a^M$ as shown in (19). In this case, the parameter a is the $y-$ degree-of-freedom of the node shown in Fig. 5 and M is the time step at the end of the step III of the thermo-mechanical programming cycle. The material parameters used for this analysis are same as listed in Table 1. The adjoint method and the forward difference method were used to evaluate the derivative of the tip displacement with respect to the mixing ratio of each element. Figure 25 shows

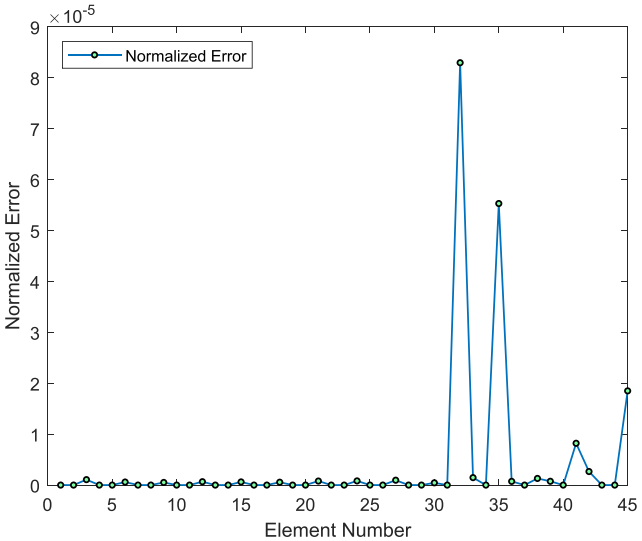

Fig. 25 Comparison between the sensitivity values evaluated through the finite-difference scheme and the adjoint formulation

Table 2 Sensitivity values evaluated through the adjoint formulation and the finite difference method

Element no.	Adjoint sensitivities	Finite difference sensitivities	Normalized error ($\times 10^{-6}$)
1	−0.2416477	−0.2416476	0.482
2	−0.0000000	−0.0000001	–
3	0.2416477	0.2416475	1.07
4	−0.2543351	−0.2543351	0.00
5	0.0000000	0.0000000	0.00
6	0.2543351	0.2543350	0.599
7	−0.2375154	−0.2375154	0.00
8	0.0000000	0.0000000	0.00
9	0.2375154	0.2375153	0.516
10	−0.2225283	−0.2225282	0.376
11	0.0000000	0.0000000	0.00
12	0.2225283	0.2225281	0.661
13	−0.2038087	−0.2038086	0.359
14	0.0000000	0.0000000	0.00
15	0.2038086	0.2038085	0.619
16	−0.1844918	−0.1844917	0.539
17	−0.0000001	−0.0000001	0.00
18	0.1844916	0.1844915	0.563
19	−0.1650572	−0.1650571	0.244
20	−0.0000010	−0.0000010	0.00
21	0.1650567	0.1650565	0.793
22	−0.1456293	−0.1456293	0.00
23	−0.0000042	−0.0000041	–
24	0.1456292	0.1456291	0.818
25	−0.1262059	−0.1262059	0.00
26	−0.0000104	−0.0000104	0.00
27	0.1262118	0.1262119	0.958
28	−0.1067716	−0.1067717	0.454
29	−0.0000017	−0.0000017	0.00
30	0.1068102	0.1068101	0.441
31	−0.0873091	−0.0873091	0.00
32	0.0001378	0.0001379	82.9
33	0.0874321	0.0874320	1.46
34	−0.0678103	−0.0678104	0.276
35	0.0008085	0.0008084	55.2
36	0.0680543	0.0680542	0.724
37	−0.0488513	−0.0488514	1.12
38	0.0027865	0.0027864	1.30
39	0.0480513	0.0480513	0.00
40	−0.0302951	−0.0302951	0.00
41	0.0042528	0.0042528	0.00
42	0.0250887	0.0250886	2.65
43	−0.0388250	−0.0388251	0.415
44	−0.0123738	−0.0123738	0.00
45	0.0027180	0.0027181	18.5

the normalized error of the sensitivity values obtained by the finite-difference approach and the adjoint sensitivity analysis. The normalized error (NE) for each element is evaluated as:

$$NE = \left| \frac{adjoint - FD}{FD} \right| \tag{B.7}$$

Note that for elements where the sensitivity is at or near zero, we have omitted the normalized error to avoid the indication of an artificially high error due to an extremely small denominator. The displacement obtained at the end of step III was -0.0130 mm. The sensitivity values obtained through the adjoint formulation and the finite-difference method are tabulated in Table 2. The maximum error between these values was found to be 2.6×10^{-7}. This established that the framework developed can successfully compute the sensitivities for SMP materials with a high degree of accuracy.

Figure 26 shows the time required to calculate $\frac{\partial \boldsymbol{R}_{n+1}}{\partial \boldsymbol{u}_{n-7}}$, the contribution of a total of 8 simulation steps, for a finite-element mesh of 50 elements by a single processor. As we can see, just using eight steps to simulate the entire SMP thermo-mechanical programming cycle even for a coarse mesh can incur high computational costs. This result motivated the development of PETSc-based parallel implementation of the FEA and sensitivity evaluation framework using CPUs on the *Golub Cluster* at the University of Illinois. Since the bottleneck for the entire algorithm is the sensitivity evaluation and particularly the time-dependent algorithm, the parallelization is done with the objective of distributing the elements onto the processors such that each processor has the optimum number of elements for efficient computations. A total of 144 processors (6 nodes with 24 processors each) were utilized for generating the 2D results. For the 3D optimization implementation, a total of 250 processors (10 nodes with 25 processors each) were utilized. The structural optimization problem is solved using the Method of Moving Asymptotes (MMA) (Svanberg 1987). The PETSc implementation of the MMA algorithm is based on the paper by Aage et al. (2015).

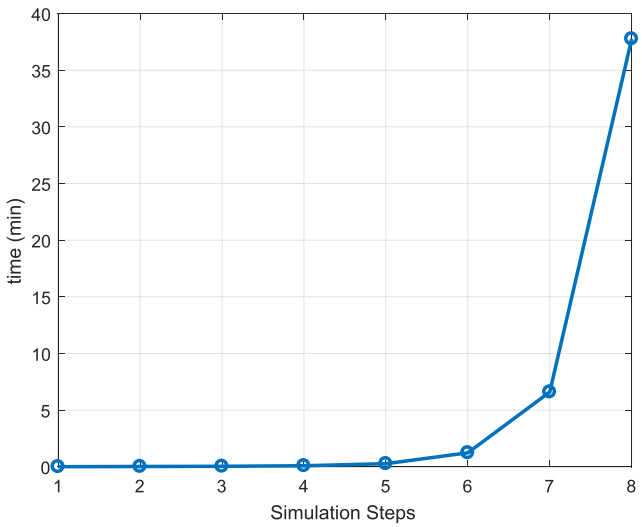

Fig. 26 Computation time required for tracking $\frac{\partial \boldsymbol{\varepsilon}_n^{ir}}{\partial \boldsymbol{\varepsilon}_{n-1}^{r}}$ terms

Appendix 3: Validation of the finite element model

After implementing the constitutive model using the finite element framework for a single shape memory polymer material with the material properties as tabulated in Table 1 for SMP^1, the accuracy of the implementation was verified against existing experimental and computational results from the literature. The results and the comparisons here are for the *full* thermomechanical programming cycle, not the modified cycle described in Fig. 3. Two broad cases, time-independent SMP behavior and time-dependent SMP behavior, were analyzed and their results were compared.

3.1 Time-independent SMP behavior

To verify the current finite element implementation, the results obtained for a time-independent *stress free strain recovery* cycle were compared with the experimental results obtained by Liu et al. (2006). Figure 27b shows that the internal stress in a SMP sample increases as the temperature is reduced. This increase in the internal stress is due to an increase in the thermal stresses since the sample cannot contract with the decrease of temperature. We can observe that near the vicinity of the glass-transition temperature, the internal stress is negligible. This can be attributed to the low thermal stresses in this region. In the regions away from the glass-transition temperature, the internal stress increases sharply due to the presence of the glassy phase. The nature of evolution of the internal stresses, as observed experimentally in Fig. 27a for different amounts of pre-strains, is captured successfully by the current implementation. The discrepancies in the magnitude of the stresses can be attributed to the different materials used in the experimental studies and the numerical simulations. The difference in the material properties arises mainly due to the fact that the current analysis is geared toward application in the topology optimization algorithm and is

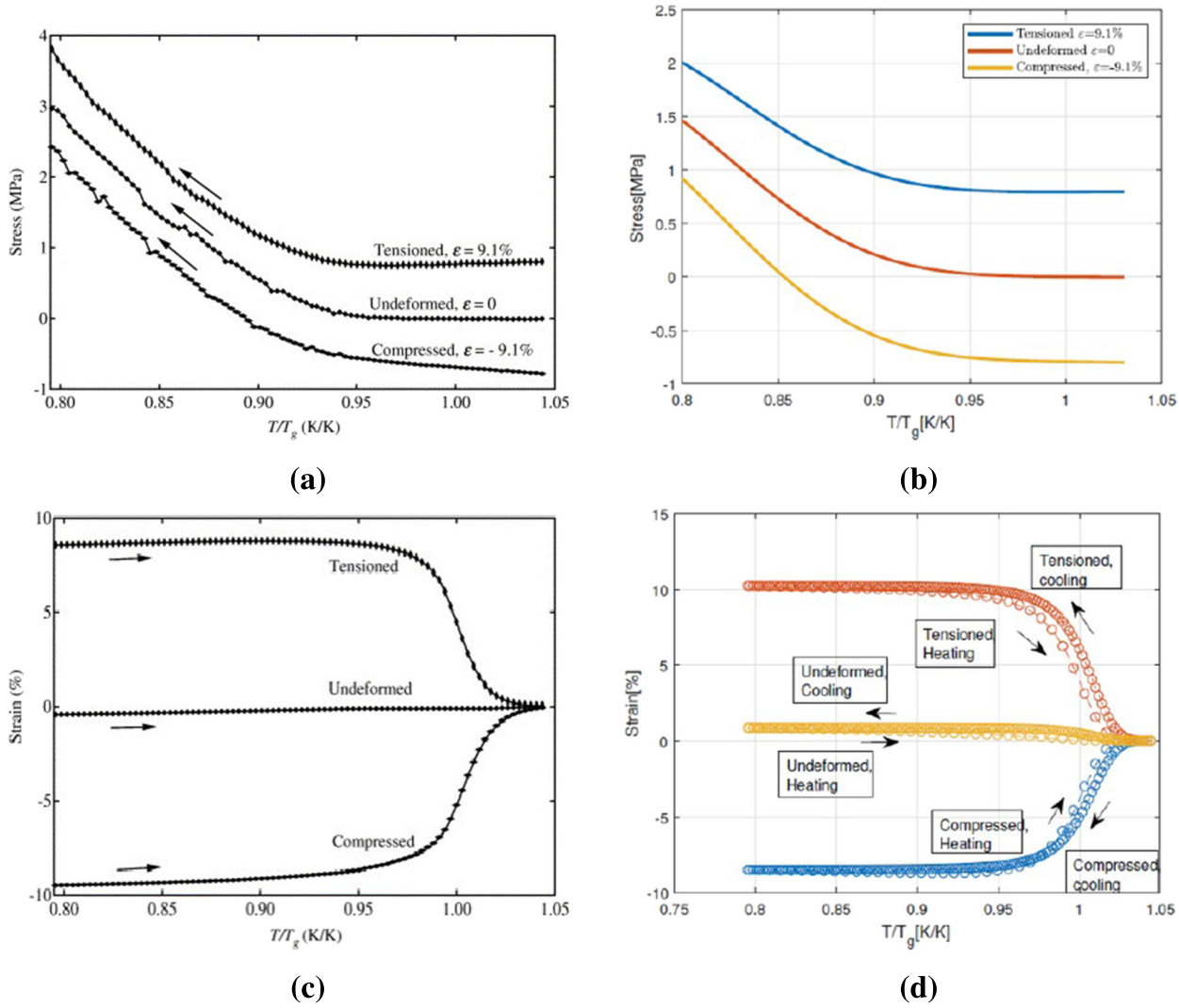

Fig. 27 **a**, **c** Experiments reported by Liu et al. (2006) for the *stress free strain recovery* cycle. **b**, **d** Results from the current FEM implementation

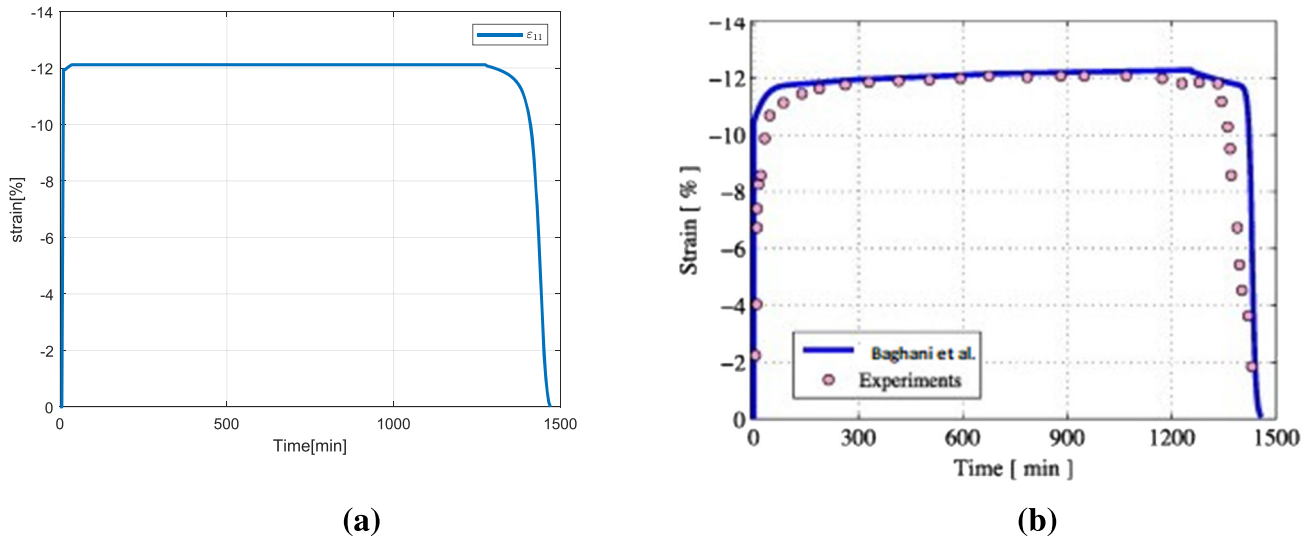

Fig. 28 **a** Reproduction of the shape memory effect (*stress free strain recovery*) as captured by the current implementation. **b** Numerical implementation done by Baghani et al. (2012) for experiments reported by Li and Nettles (2010)

based on the rheological model as shown in Fig. 2, where the material properties used for the different components are as per the values tabulated in Table 4 of ref. Baghani et al. (2012), which are different from the material properties reported in the experiments. This analysis was carried out to demonstrate that the current formulation can identify and mimic the nature of stress-strain evolution as observed in experimental results.

Figure 27d shows the free strain recovery for different amounts of fixed pre-strains with increase in temperature. As the temperature is increased, the amount of strains stored in the SMP sample decreases and the structure comes back to its initial configuration. It can be observed that even for different types of deformations, the paths followed during the recovery process are similar. The results obtained by the current implementation closely resemble the experimental results as shown in Fig. 27c. These results show that the current finite-element implementation can correctly capture the time-independent nature of the stress and strain evolution for a SMP material.

3.2 Time-dependent SMP behavior

The experiment performed by Li and Nettles (2010) was computationally simulated to validate the time-dependent aspect of the current implementation. Here, an SMP-based foam was compressed under a constant stress, held for 30 min and was subjected to the thermo-mechanical cycle. The main objective is to analyze the nature and form of the strain-time behavior. A comparison of the results of the current implementation with the numerical studies reported by Baghani et al. (2012) is shown in Fig. 28. Note that the

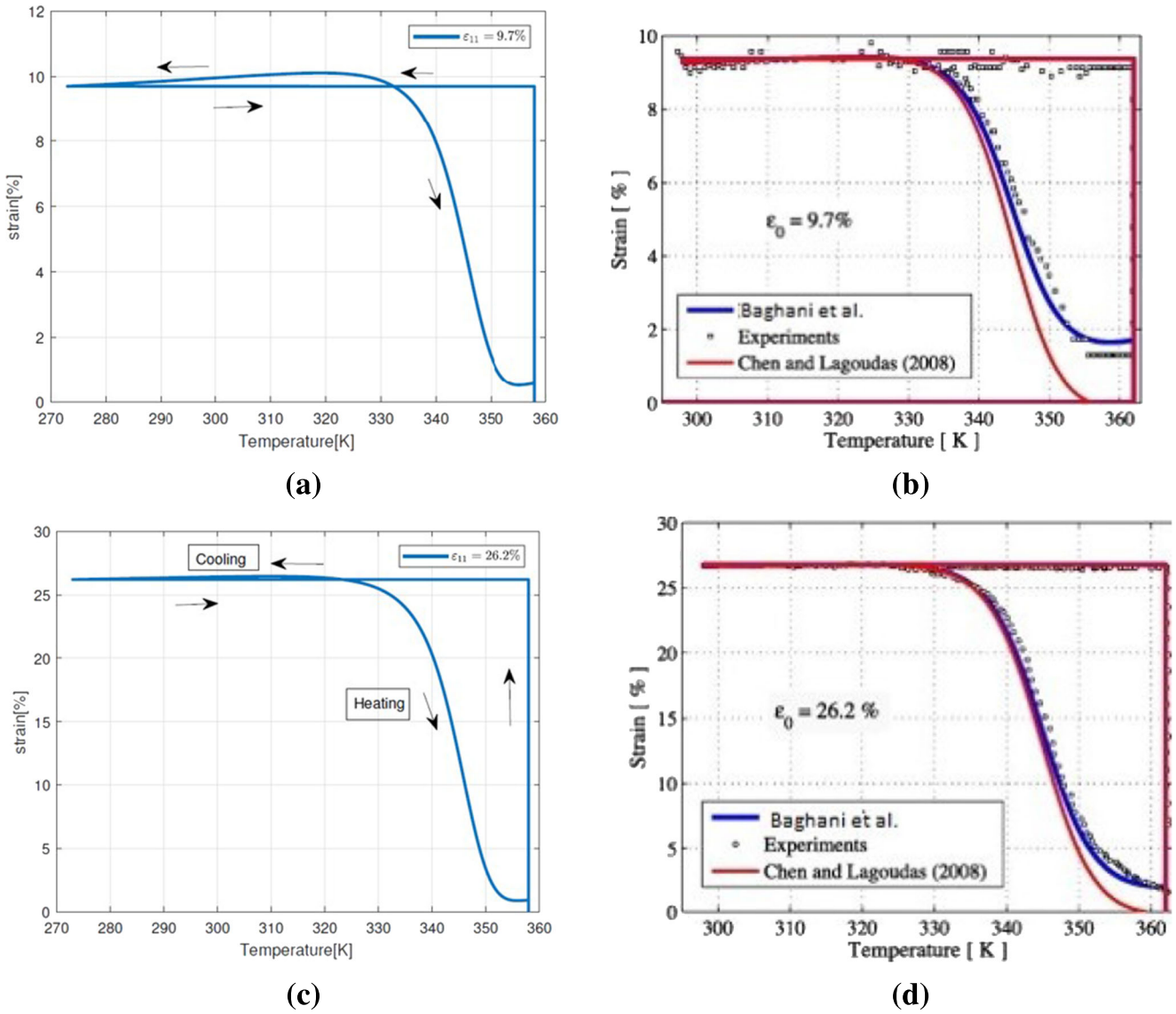

Fig. 29 **a**, **c** SMP simulation for uniaxial tensile strain of 9.7% and 26.2% respectively. **b**, **d** Experiments reported by Volk et al. (2010) (dotted data points), numerical implementation of Chen and Lagoudas (2008b) and Baghani et al. (2012)

deviations observed in Fig. 28a from those in Fig. 28b are mainly due to the use of different thermal strain function. We have used the function of thermal strain as given by (8) to maintain a continuity in our implementation. Also, the material parameters used differ in the two cases since we have not included any hard phase. Since our objective was to show that the current implementation sufficiently captures the SMP mechanics fit for moving forward with the topology optimization design, we can conclude that the overall correlation between the experimental results and the current implementation agrees to a level sufficient for our implementation.

Figure 29 compares the current implementation with the experiments reported by Volk et al. (2010) regarding the time-dependent uniaxial loading of SMPs followed by the thermo-mechanical cycle. We also compare our results with the implementation of Baghani et al. (2012). The results show that the current implementation can successfully capture the time-dependent effects with a moderate level of irreversible strains. From Fig. 29, we can observe that the strain at $T = T_H$ is not 0, i.e., we do not recover all the strain that is put into the structure while it is deformed. This is due to the fact that while applying deformation a part of the total strain, irreversible strain component($\boldsymbol{\varepsilon}^i$), is permanently lost and cannot be recovered.

Figure 30 contains results from simulation of the multiaxial loading of an SMP material and compares the temperature vs. strain and time vs. strain plots obtained

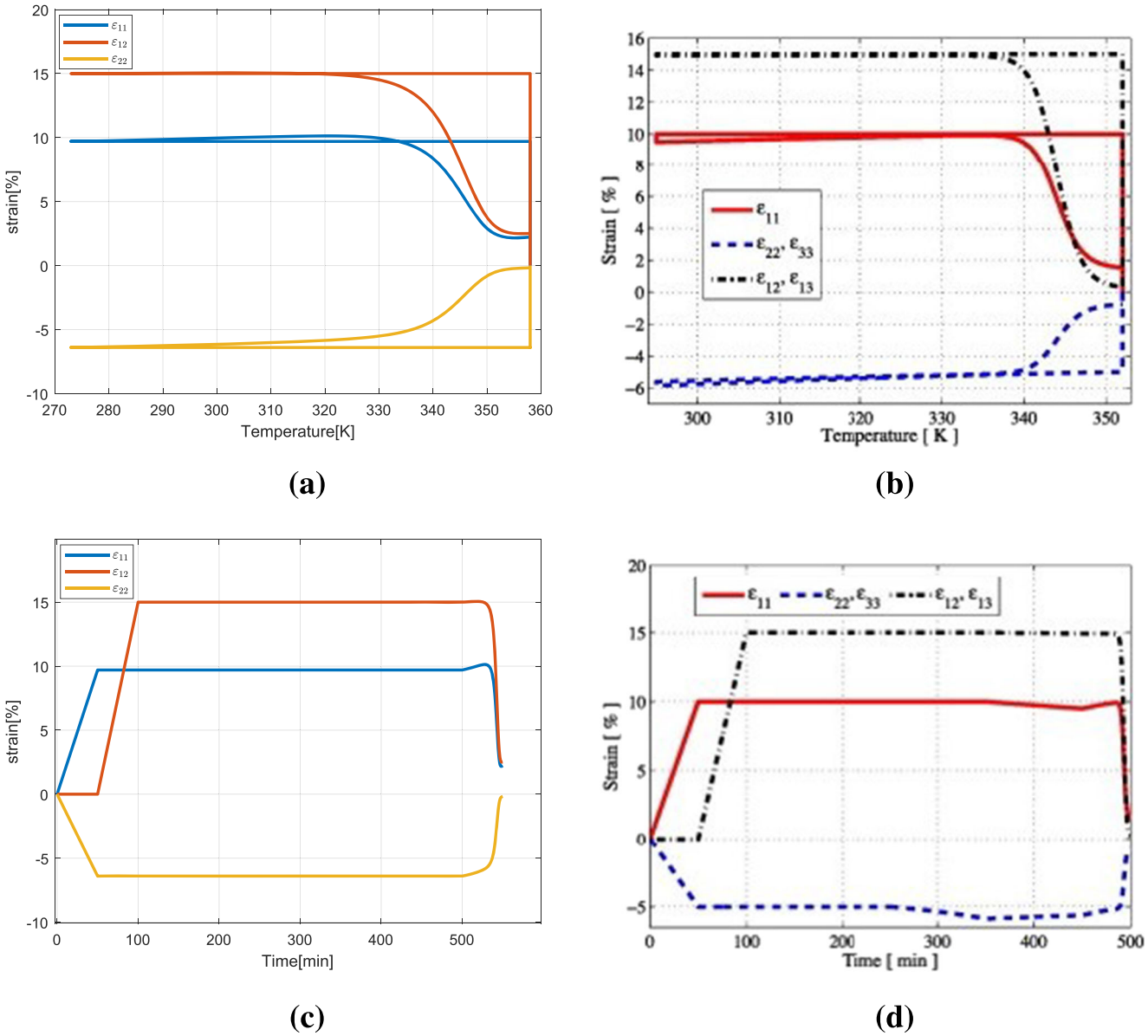

Fig. 30 **a**, **c** Results captured by the current implementation. **b**, **d** Simulation results reported by Baghani et al. (2012) for multiaxial loading of an SMP material

from the current implementation with the results reported by Baghani et al. (2012). The similarity of the results indicates that the current implementation can successfully capture the multiaxial loading of SMPs.

Having verified that the current finite element implementation of the constitutive model proposed by Baghani et al. (2012) can capture the essential characteristics of SMPs to an acceptable level of accuracy, we move forward with the computational design aspect using topology optimization.

Appendix 4: The symmetry assumption

The results in Section 6.2 assume a symmetric design due to the symmetry of the loading and boundary conditions. To verify the assumption, we have also solved the problem using the full domain. Figure 32 shows the optimized material distribution for the self-actuating gripper corresponding to the full-design domain as shown in Fig. 31a without the assumption of symmetry.

The optimization problem statement for the full-domain case is written as:

$$\begin{aligned} \underset{\boldsymbol{\rho}}{\text{minimize}} \quad & -({U_y}^b - {U_y}^t)|_{t=T^*} \\ \text{subject to} \quad & V_{SMP^1}(\boldsymbol{\rho}) \leq V_{SMP^1}^{Max}, \quad 0 \leq \boldsymbol{\rho} \leq 1 \end{aligned} \tag{D.1}$$

The optimized value of ${U_y}^N$ for the same node and under the same loading conditions is 2.2758 mm, in the negative y-direction. If we compare the optimized material distribution for the half-domain case as shown in Fig. 14 and the full-domain case as shown in Fig. 32, we observe that the two results have very similar topologies, with minor differences in the material distributions. The differences between the two solutions can be explained by the nonconvex nature of the optimization problem, which makes the optimization solutions dependent on both the starting point (initial guess) of the optimization, the search path followed to arrive at the final solution.

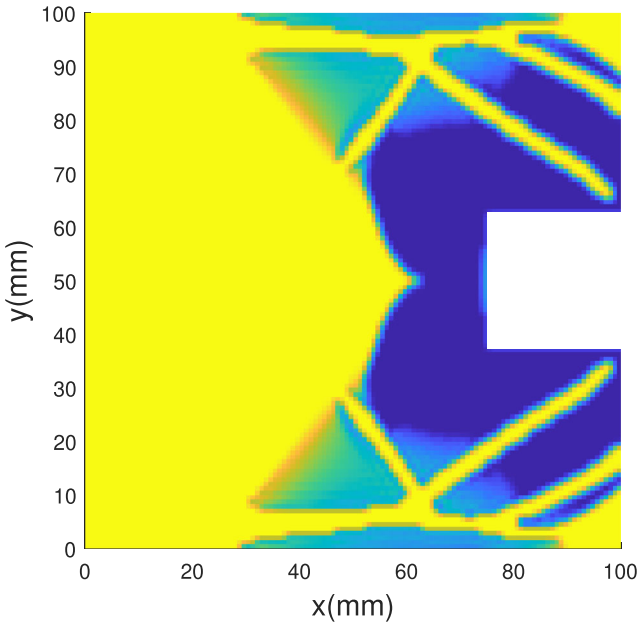

Fig. 32 Optimized material distribution for the self-actuating gripper for the full-design domain

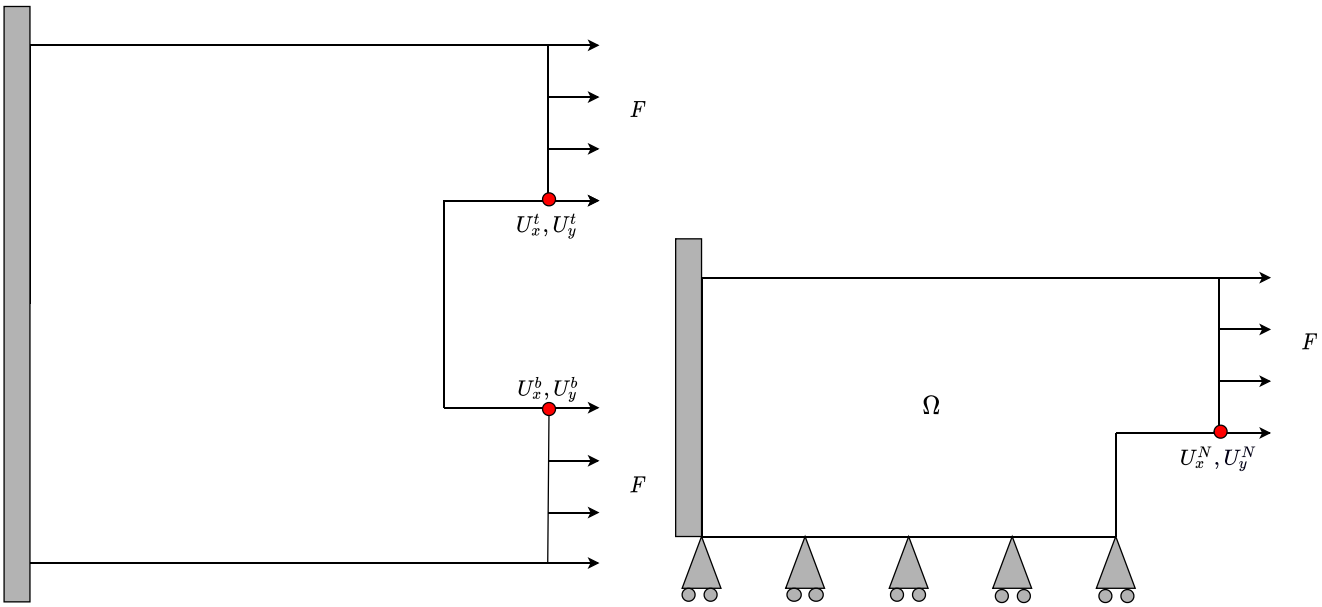

(a) Full domain **(b)** Half domain

Fig. 31 Boundary conditions for the gripper optimization problem with full and half domains

References

Aage N, Andreassen E, Lazarov BS (2015) Topology optimization using PETSc: an easy-to-use, fully parallel, open source topology optimization framework. Struct Multidiscip Optim 51(3):565–572

Baghani M, Naghdabadi R, Arghavani J, Sohrabpour S (2012) A thermodynamically-consistent 3D constitutive model for shape memory polymers. Int J Plast 35:13–30. [Online]. Available: http://www.sciencedirect.com/science/article/pii/S0749641912000083

Behl M, Lendlein A (2011) Shape-memory polymers, pp. 1–16. American Cancer Society, [Online]. Available: https://onlinelibrary.wiley.com/doi/abs/10.1002/0471238961.1908011612051404.a01.pub2

Bowen CR, Kim HA, Weaver PM, Dunn S (2014) Piezoelectric and ferroelectric materials and structures for energy harvesting applications. Energy Environ Sci 7:25–44. [Online]. Available: https://doi.org/10.1039/C3EE42454E

Bendsøe MP, Sigmund O (1999) Material interpolation schemes in topology optimization. Arch Appl Mech 69(9):635–654. [Online]. Available: https://doi.org/10.1007/s004190050248

Bruns TE, Tortorelli DA (2001) Topology optimization of non-linear elastic structures and compliant mechanisms. Comput Methods Appl Mech Eng 190(26):3443–3459. [Online]. Available: http://www.sciencedirect.com/science/article/pii/S0045782500002784

Carbonari RC, Silva ECN, Paulino GH (2008) Topology optimization applied to the design of functionally graded piezoelectric bimorph. AIP Conf Proc 1:291–296. [Online]. Available: https://aip.scitation.org/doi/abs/10.1063/1.2896793

Carrell J, Tate D, Wang S, Zhang H-C (2011) Shape memory polymer snap-fits for active disassembly. J Clean Prod 19(17):2066–2074. [Online]. Available: http://www.sciencedirect.com/science/article/pii/S0959652611002393

Chen Y-C, Lagoudas DC (2008a) A constitutive theory for shape memory polymers. Part I: large deformations. J Mech Phys Solids 56(5):1752–1765. [Online]. Available: http://www.sciencedirect.com/science/article/pii/S0022509607002323

Chen Y-C, Lagoudas DC (2008b) A constitutive theory for shape memory polymers. Part II: a linearized model for small deformations. J Mech Phys Solids 56(5):1766–1778. [Online]. Available: http://www.sciencedirect.com/science/article/pii/S0022509607002311

Cho J-H, Azam A, Gracias DH (2010) Three dimensional nanofabrication using surface forces. Langmuir 26(21):16534–16539. pMID: 20507147. [Online]. Available: https://doi.org/10.1021/la1013889

Choi M-J, Cho S (2018) Isogeometric configuration design optimization of shape memory polymer curved beam structures for extremal negative Poisson's ratio. Struct Multidiscip Optim 58(5):1861–1883. [Online]. Available: https://doi.org/10.1007/s00158-018-2088-y

Frecker MI (2003) Recent advances in optimization of smart structures and actuators. J Intell Mater Syst Struct 14(4–5):207–216. [Online]. Available: https://doi.org/10.1177/1045389X03031062

Gaynor AT, Meisel NA, Williams CB, Guest JK (2014) Multiple-material topology optimization of compliant mechanisms created via polyjet three-dimensional printing. J Manuf Sci Eng 136(6):061015–061015–10. [Online]. Available: https://doi.org/10.1115/1.4028439

Ge Q, Dunn CK, Qi HJ, Dunn ML (2014) Active origami by 4D printing. Smart Mater Struct 23(9):094007

Ge Q, Sakhaei AH, Lee H, Dunn CK, Fang NX, Dunn ML (2016) Multimaterial 4D printing with tailorable shape memory polymers. Sci Rep 6:31110 EP. [Online]. Available: https://doi.org/10.1038/srep31110

Geiss MJ, Maute K (2018) Topology optimization of active structures using a higher-order level-set-XFEM-density approach. In: 2018 Multidisciplinary analysis and optimization conference, p 4053

Geiss MJ, Boddeti N, Weeger O, Maute K, Dunn ML (2019) Combined level-set-XFEM-density topology optimization of four-dimensional printed structures undergoing large deformation. J Mech Des 5:141

James KA, Waisman H (2015) Topology optimization of viscoelastic structures using a time-dependent adjoint method. Comput Methods Appl Mech Eng 285:166–187. [Online]. Available: http://www.sciencedirect.com/science/article/pii/S004578251400437X

Langelaar M, van Keulen F (2008) Modeling of shape memory alloy shells for design optimization. Comput Struct 86(9):955–963

Langelaar M, Yoon GH, Kim Y, Van Keulen F (2011) Topology optimization of planar shape memory alloy thermal actuators using element connectivity parameterization. Int J Numer Methods Eng 88(9):817–840

Lendlein A, Jiang H, Jünger O, Langer R (2005) Light-induced shape-memory polymers. Nature 434(7035):879–882. [Online]. Available: https://doi.org/10.1038/nature03496

Leng J, Yu K, Liu Y (2010) Recent progress of smart composite material in HIT. [Online]. Available: https://doi.org/10.1117/12.854803

Li G, Nettles D (2010) Thermomechanical characterization of a shape memory polymer based self-repairing syntactic foam. Polymer 51(3):755–762. http://www.sciencedirect.com/science/article/pii/S0032386109010672

Liu Y, Gall K, Dunn ML, Greenberg AR, Diani J (2006) Thermomechanics of shape memory polymers: uniaxial experiments and constitutive modeling. Int J Plast 22(2):279–313. [Online]. Available: http://www.sciencedirect.com/science/article/pii/S0749641905000604

Liu Y, Du H, Liu L, Leng J (2014) Shape memory polymers and their composites in aerospace applications: a review. Smart Mater Struct 23(2):023001. [Online]. Available: https://doi.org/10.1088/0964-1726/23/2/023001

Maute K, Tkachuk A, Wu J, Jerry Qi H, Ding Z, Dunn ML (1402) Level set topology optimization of printed active composites. J Mech Des 2015(11):10. [Online]. Available: https://doi.org/10.1115/1.4030994

Oliver K, Seddon A, Trask RS (2016) Morphing in nature and beyond: a review of natural and synthetic shape-changing materials and mechanisms. J Mater Sci 51(24):10663–10689. [Online]. Available: https://doi.org/10.1007/s10853-016-0295-8

Qi HJ, Nguyen TD, Castro F, Yakacki CM, Shandas R (2008) Finite deformation thermo-mechanical behavior of thermally induced shape memory polymers. J Mech Phys Solids 56(5):1730–1751. [Online]. Available: http://www.sciencedirect.com/science/article/pii/S002250960700230X

Reed JL Jr, Hemmelgarn CD, Pelley BM, Havens E (2005) Adaptive wing structures. [Online]. Available: https://doi.org/10.1117/12.599922

Reese S, Böl M, Christ D (2010) Finite element-based multiphase modelling of shape memory polymer stents. Comput Methods Appl Mech Eng 199(21):1276–1286. Multiscale models and mathematical aspects in solid and fluid mechanics. [Online]. Available: http://www.sciencedirect.com/science/article/pii/S004578250900262X

Rupp CJ, Evgrafov A, Maute K, Dunn ML (2009) Design of piezoelectric energy harvesting systems: a topology optimization approach based on multilayer plates and shells. J Intell Mater Syst Struct 20(16):1923–1939. [Online]. Available: https://doi.org/10.1177/1045389X09341200

Svanberg K (1987) The method of moving asymptotes—a new method for structural optimization. Int J Numer Methods Eng 24(2):359–

373. [Online]. Available: https://onlinelibrary.wiley.com/doi/abs/10.1002/nme.1620240207

Siéfert E, Reyssat E, Bico J, Roman B (2019) Bio-inspired pneumatic shape-morphing elastomers. Nat Mater 18(1):24–28. [Online]. Available: https://doi.org/10.1038/s41563-018-0219-x

Sigmund O, Torquato S (1999) Design of smart composite materials using topology optimization. Smart Mater Struct 8(3):365–379. [Online]. Available: https://doi.org/10.1088/0964-1726/8/3/308

Silva ECN, Kikuchi N (1999) Design of piezoelectric transducers using topology optimization. Smart Mater Struct 8(3):350–364. [Online]. Available: https://doi.org/10.1088/0964-1726/8/3/307

Tibbits S (2014) 4D printing: multi-material shape change. Archit Des 84(1):116–121. [Online]. Available: https://onlinelibrary.wiley.com/doi/abs/10.1002/ad.1710

Volk BL, Lagoudas DC, Chen Y-C, Whitley KS (2010) Analysis of the finite deformation response of shape memory polymers: I. Thermomechanical characterization. Smart Mater Struct 19(7):075005

Volk BL, Lagoudas DC, Maitland DJ (2011) Characterizing and modeling the free recovery and constrained recovery behavior of a polyurethane shape memory polymer. Smart Mater Struct 20(9):094004. [Online]. Available: https://doi.org/10.1088/0964-1726/20/9/094004

Wache HM, Tartakowska DJ, Hentrich A, Wagner MH (2003) Development of a polymer stent with shape memory effect as a drug delivery system. J Mater Sci: Mater Med 14(2):109–112. [Online]. Available: https://doi.org/10.1023/A:1022007510352

Yin L, Ananthasuresh G (2002) A novel topology design scheme for the multi-physics problems of electro-thermally actuated compliant micromechanisms. Sens Actuat A: Phys 97–98:599–609. Selected papers from Eurosenors XV. [Online]. Available: http://www.sciencedirect.com/science/article/pii/S0924424701008536

Yu K, Yin W, Sun S, Liu Y, Leng J (2009) Design and analysis of morphing wing based on SMP composite. [Online]. Available: https://doi.org/10.1117/12.815712